Theoretical and Applied Fracture Mechanics 107 (2020) 102550

Contents lists available at ScienceDirect

Theoretical and Applied Fracture Mechanics

journal homepage: www.elsevier.com/locate/tafmec

The phase-field approach to self-healable fracture of elastomers: A model accounting for fracture nucleation at large, with application to a class of conspicuous experiments

Aditya Kumar, Oscar Lopez-Pamies*

Department of Civil and Environmental Engineering, University of Illinois, Urbana–Champaign, IL 61801, USA

ARTICLE INFO

Keywords:
Cavitation
Strength
Self-healing polymers
Finite deformations
Non-conforming finite elements

ABSTRACT

In a recent contribution, Kumar et al. (2018) have introduced a phase-field formulation and associated numerical implementation aimed at modeling the nucleation and propagation of fracture and healing in elastomers undergoing arbitrarily large quasistatic deformations, phenomena that have come into clear focus thanks to new experiments carried out at high spatiotemporal resolution (Poulain et al., 2017; 2018). With the object of explaining the nucleation of internal fracture observed in those experiments, Kumar et al. (2018) also provided a specific model within the general formulation that accounted for fracture nucleation at material points in the bulk that are subject to purely hydrostatic stress. The first of two objectives of this paper is to introduce a complete model within the general formulation that accounts for fracture nucleation at large, be it within the bulk (under arbitrary states of stress, not just hydrostatic), from large pre-existing cracks, small pre-existing cracks, or from smooth and non-smooth boundary points.

The second objective is to showcase the capabilities of the proposed complete model by deploying it to simulate the nucleation and propagation of fracture in a class of conspicuous experiments, that of rubber bands subject to tensile loading. Specifically, 3D simulations are presented of very short, short, and long rubber bands under tension, which are representative of two famed experiments known to feature very different — and, for the cases of the very short and the short rubber bands, very complex — types of nucleation and propagation of fracture.

1. Introduction

Investigations of both the *nucleation* and *propagation* of fracture in elastomers subject to externally applied mechanical loads have been intensely pursued for over a century, but mostly as separate subjects; see, e.g., the review articles of Busse [6] and Gent and Mars [17]. In a recent contribution, *per contra*, the experiments of Poulain et al. [37,38] have indicated that to convincingly understand both processes, it is imperative to consider them together from a unifying point of view. Those experiments have further revealed that fracture that nucleates internally within the bulk of elastomers can self-heal. The process of *healing*, being in a sense one and the same as the process of fracture, must too be considered together with nucleation and propagation of fracture on an equal footing in order to ultimately reach a complete understanding of the fracture mechanics of elastomers.

In this context, Kumar et al. [23] have introduced a regularized theory of fracture — of phase-field type — that views the nucleation and propagation of fracture as well as the possibility of healing as three intertwined parts of the same phenomenon. The theory can be thought of as a generalization of the phase-field regularization [4,5] of the variational theory of brittle fracture of Francfort and Marigo [11] in that it modifies the former on two counts, one pertaining to nucleation, the other to healing[1]. The generalization goes as follows.

Recall first that for a nonlinear elastic solid with stored-energy function $\mathcal{W}(\mathbf{F})$ and critical elastic energy release rate G_c occupying an open bounded domain $\Omega_0 \in \mathbb{R}^3$ in its undeformed and stress-free configuration, with boundary $\partial\Omega_0$ and unit outward normal $\mathbf{N}$, the standard phase-field approximation of the variational theory of Francfort and Marigo [11] amounts to considering the class of minimization problems, written here discretely in time for simplicity,

* Corresponding author.
E-mail addresses: akumar51@illinois.edu (A. Kumar), pamies@illinois.edu (O. Lopez-Pamies).

[1] Alternatively, the theory can also be viewed as a phase transition of Allen–Cahn type [24].

https://doi.org/10.1016/j.tafmec.2020.102550

Available online 25 February 2020
0167-8442/ © 2020 The Authors. Published by Elsevier Ltd. This is an open access article under the CC BY-NC-ND license (http://creativecommons.org/licenses/BY-NC-ND/4.0/).

$$\min_{\substack{\mathbf{y}=\bar{\mathbf{y}}(\mathbf{X},t_k)\,\text{on}\,\partial\Omega_0^{\mathcal{D}} \\ 0\leqslant z\leqslant z_{k-1}\leqslant 1}} \mathcal{E}^{\varepsilon}(\mathbf{y},z) := \int_{\Omega_0}\psi(z)\mathcal{W}(\mathbf{F}(\mathbf{y}))\mathrm{d}\mathbf{X} - \mathcal{P}(t_k) + \frac{G_c}{4c_s}\int_{\Omega_0}\left(\frac{s(z)}{\varepsilon}+\varepsilon\nabla z\cdot\nabla z\right)\mathrm{d}\mathbf{X} \tag{1}$$

with

$$\mathcal{P}(t_k) = \int_{\Omega_0}\mathbf{b}(\mathbf{X},t_k)\cdot\mathbf{y}\,\mathrm{d}\mathbf{X} + \int_{\partial\Omega_0^{\mathcal{N}}}\bar{\mathbf{t}}(\mathbf{X},t_k)\cdot\mathbf{y}\,\mathrm{d}\mathbf{X}$$

for the deformation field $\mathbf{y}(\mathbf{X},t)$ and phase field $z(\mathbf{X},t)$ within Ω_0 at any given discrete time $t_k \in \{0=t_0, t_1, ..., t_m, t_{m+1}, ..., t_M=T\}$. In these expressions, $\partial\Omega_0^{\mathcal{D}}$ is the part of the boundary $\partial\Omega_0$ where a deformation $\bar{\mathbf{y}}(\mathbf{X},t_k)$ is prescribed, $\partial\Omega_0^{\mathcal{N}}=\partial\Omega_0\backslash\partial\Omega_0^{\mathcal{D}}$ is its complementary part where a nominal traction $\bar{\mathbf{t}}(\mathbf{X},t_k)$ is prescribed, $\mathbf{b}(\mathbf{X},t_k)$ stands for a body force, $\mathbf{F}(\mathbf{y}):=\nabla\mathbf{y}$ denotes the gradient of the deformation field $\mathbf{y}$, $\varepsilon>0$ is a regularization or localization length, ψ and s are continuous monotonic functions such that $\psi(0)=0$, $\psi(1)=1$, $s(0)=1$, $s(1)=0$, and $c_s:=\int_0^1\sqrt{s(z)}\mathrm{d}z$ is a normalization parameter. Note that the phase field z takes values in $[0,1]$ and that $z=1$ identifies regions of the sound elastomer, whereas $z=0$ identifies regions of the elastomer that have been fractured.

Although more comparisons with experiments should be carried out, there is already strong evidence that the phase-field formulation (1) provides an accurate description of the propagation of cracks in elastomers under arbitrary quasistatic loading conditions, so long as viscous dissipation is small and there is no strain crystallization so that the behavior of the elastomers is predominantly elastic. By contrast, it is now well understood that the phase-field formulation[2] (1) cannot properly describe fracture nucleation, irrespectively of the choice of functions $\psi(z)$, $s(z)$, and value of the localization length ε. This is because the formulation (1) is purely energetic and as a result it cannot account for one essential ingredient that is not energetic, but rather stress-based: *the strength of the elastomer*; see Section 3.1 in Kumar et al. [23], Kumar et al. [25], and Section 3 below. Furthermore, the formulation (1) describes fracture as an irreversible and purely dissipative process ruling out thus the possibility of healing. Kumar et al. [23] proposed alterations to (1) that circumvent these limitations on nucleation and healing while keeping undisturbed the proven ability of (1) to model crack propagation. Roughly speaking, the idea behind the phase-field framework proposed in Kumar et al. [23] amounts:

- to consider the Euler–Lagrange equations of (1) — and not the variational principle (1) itself — as the primal model,
- to add an external driving force c_e in the Euler–Lagrange equation governing the evolution of the phase field z that represents the macroscopic manifestation of the presence of the inherent microscopic defects in the elastomer and hence that brings into the model direct dependence on its strength, and
- to remove the irreversibility constraint on the phase field z by introducing a critical energy release rate or toughness with two branches, $k(\dot{z})=k_{\mathcal{F}}=G_c$ if $\dot{z}\leqslant 0$ and $k_{\mathcal{H}}$ if $\dot{z}>0$, one to describe fracture, the other to describe healing.

The precise mathematical formulation of the framework is spelled out below in Section 2. In their original work, aimed at explaining the nucleation of internal fracture observed in the experiments of Poulain et al. [37,38], Kumar et al. [23] also proposed a specific constitutive prescription for the external driving force c_e that restricted attention to accounting for the strength of the given elastomer of interest only under hydrostatic stress. The first objective of this paper is to introduce a complete constitutive prescription for c_e that accounts for the entire strength of the elastomer under arbitrary stress states. The resulting phase-field model is thus one capable of describing fracture nucleation at large, be it within the bulk (under arbitrary states of stress, not just hydrostatic), from large pre-existing cracks, small pre-existing cracks, or from smooth and non-smooth boundary points. This new external driving force c_e is presented in Section 4, following an instructive recap in Section 3 of all the various ways in which fracture can nucleate in elastomers. The second objective of this paper is to demonstrate the capabilities of the proposed complete model by examining via full 3D simulations its predictions for the nucleation and propagation of fracture in a class of conspicuous experiments, that of rubber bands subject to tensile loading. Specifically, Section 5 presents simulations on very short, short, and long rubber bands of initially circular cross section. The very short and short rubber bands correspond to the so-called poker-chip specimens studied experimentally by many, see, e.g., the classical works of Busse [6], Gent and Lindley [15], and Lindsey [29]. The long rubber bands, on the other hand, are representative of the celebrated specimens — invented by Stephen Perry in the 1840s — that most of us have used and played with since childhood.

2. The phase-field formulation of Kumar et al. (2018)

As outlined in the Introduction, the phase-field formulation of Kumar et al. [23] is not based on a variational principle but, instead, on a coupled system of nonlinear PDEs (partial differential equations) that governs the evolution of the deformation field $\mathbf{y}(\mathbf{X},t)$ and the phase field $z(\mathbf{X},t)$. Those PDEs correspond to a time-continuous version of the Euler–Lagrange equations of the variational problem (1), for the choice of degradation and surface localization functions

$$\psi(z)=z^2 \qquad \text{and} \qquad s(z)=1-z, \tag{2}$$

that include the presence of an external driving force

$$c_e(\mathbf{X},t), \qquad (\mathbf{X},t)\in\Omega_0\times[0,T] \tag{3}$$

in the Euler–Lagrange equation for the phase field $z(\mathbf{X},t)$ and that introduce a two-branch toughness featuring possibly different critical energy release rates for fracture ($\dot{z}<0$) and for healing ($\dot{z}>0$):

$$k(\dot{z})=\begin{cases}k_{\mathcal{F}}=G_c & \text{if} \quad \dot{z}\leqslant 0\\ k_{\mathcal{H}} & \text{if} \quad \dot{z}>0\end{cases} \tag{4}$$

with $\dot{z}(\mathbf{X},t):=\partial z(\mathbf{X},t)/\partial t$. Precisely, taking $\mathbf{y}(\mathbf{X},0)=\mathbf{X}$ and $z(\mathbf{X},0)=1$ and rewriting (without loss in generality) the stored-energy function describing the elasticity of the elastomer in the form

$$\mathcal{W}(\mathbf{F})=W(\mathbf{F})+\kappa g(\mathbf{F}), \tag{5}$$

the governing PDEs for $\mathbf{y}(\mathbf{X},t)$ and $z(\mathbf{X},t)$ read as

$$\begin{cases}\mathrm{Div}\left[(z^2+\eta_W)\frac{\partial W}{\partial\mathbf{F}}(\nabla\mathbf{y})+(z^2+\eta_\kappa)\kappa\frac{\partial g}{\partial\mathbf{F}}(\nabla\mathbf{y})\right]+\mathbf{b}(\mathbf{X},t)=\mathbf{0},\\ (\mathbf{X},t)\in\Omega_0\times[0,T]\\ \det\nabla\mathbf{y}(\mathbf{X},t)>0, \quad (\mathbf{X},t)\in\Omega_0\times[0,T]\\ \mathbf{y}(\mathbf{X},t)=\bar{\mathbf{y}}(\mathbf{X},t), \quad (\mathbf{X},t)\in\partial\Omega_0^{\mathcal{D}}\times[0,T]\\ \left[(z^2+\eta_W)\frac{\partial W}{\partial\mathbf{F}}(\nabla\mathbf{y})+(z^2+\eta_\kappa)\kappa\frac{\partial g}{\partial\mathbf{F}}(\nabla\mathbf{y})\right]\mathbf{N}=\bar{\mathbf{t}}(\mathbf{X},t),\\ (\mathbf{X},t)\in\partial\Omega_0^{\mathcal{N}}\times[0,T]\end{cases} \tag{6}$$

and

$$\begin{cases}\mathrm{Div}[\varepsilon k(\dot{z})\nabla z]=(\text{resp. }\geqslant)\frac{8}{3}z(W(\nabla\mathbf{y})+\kappa g(\nabla\mathbf{y}))-\frac{4}{3}c_e(\mathbf{X},t)-\frac{k(\dot{z})}{2\varepsilon},\\ \text{if} \quad 0<z(\mathbf{X},t)<1 \text{ and } \dot{z}(\mathbf{X},t)\neq 0(\text{resp. }=0), \ (\mathbf{X},t)\in\Omega_0\times[0,T]\\ \mathrm{Div}[\varepsilon k(\dot{z})\nabla z]\geqslant(\text{resp. }\leqslant)\frac{8}{3}z(W(\nabla\mathbf{y})+\kappa g(\nabla\mathbf{y}))-\frac{4}{3}c_e(\mathbf{X},t)-\frac{k(\dot{z})}{2\varepsilon},\\ \text{if} \quad z(\mathbf{X},t)=1(\text{resp.}=0), \quad (\mathbf{X},t)\in\Omega_0\times[0,T]\\ \nabla z\cdot\mathbf{N}=0, \quad (\mathbf{X},t)\in\partial\Omega_0\times[0,T]\end{cases} \tag{7}$$

[2] The same shortcoming is shared by the broader class of formulations where only a "tensile" part $\mathcal{W}^+(\mathbf{F}(\mathbf{y}))$ of the elastic energy $\mathcal{W}(\mathbf{F}(\mathbf{y}))$ is multiplied by the degradation function $\psi(z)$; see, e.g., Amor et al. [2], Miehe et al. [32], Chambolle et al. [7].

Remark 1. *The degradation and surface localization functions* $\psi(z)$ *and* $s(z)$. The choice of degradation function $(2)_1$ is just one among many possible choices. It is a choice, nonetheless, that has the advantage of being mathematically simple and that has been tested thoroughly in the literature. On the other hand, the surface localization function $(2)_2$ is not just a choice among many, but it is one with unique merits. Specifically, beyond being mathematically simple, it leads to sharp and localized transitions of the phase-field variable from $z = 1$ to $z = 0$ and thus its interpretation in terms of sharp cracks is straightforward even for a finite value of the localization length ε, and not only in the limit of $\varepsilon \searrow 0$; see Pham et al. [36] and Sicsic and Marigo [40]. The specific combination (2) is sometimes labeled as `AT1`, `AT` referring to the work of Ambrosio and Tortorelli [1] and `1` for the exponent 1 for the term $(1 - z)$.

Remark 2. *The external driving force* $c_e(\mathbf{X}, t)$. Physically, the external driving force (3) represents the macroscopic manifestation of the presence of the inherent microscopic defects in the elastomer. It is hence the quantity that allow us to incorporate the strength of the elastomer into the model. For clarity, the details of how this is actually done are deferred to Section 4 below, after spelling out in Section 3 the precise and general concept of strength alongside other basic ingredients for the modeling of fracture nucleation in elastomers.

Remark 3. *The toughness function* $k(\dot{z})$. The first branch in the toughness function (4) states that the propagation of fracture progresses according to the critical energy release rate G_c of the elastomer. The second branch, on the other hand, states that such a propagation of fracture is not necessarily a purely dissipative and irreversible process. Instead, cracks can heal so long as the healing toughness $0 < k_{\mathcal{H}} \leqslant G_c$. The classical assumption of fracture irreversibility is recovered by setting $k_{\mathcal{H}} \leqslant 0$; for the "sharp-theory" view of the healing toughness $k_{\mathcal{H}}$, see Francfort et al. [12]. As elaborated in Section 3.2 of Kumar et al. [23], the two branches in (4) can be generalized to be material functions of the cumulative history of fracture and healing as opposed to just material parameters. The simulations presented below do not require such a level of generality and hence we take G_c and $k_{\mathcal{H}}$ to be material parameters here.

Remark 4. *The form (5) of the stored-energy function* $\mathcal{W}(\mathbf{F})$ *and the parameters* η_W *and* η_κ. The parameter κ in (5) is a non-negative material parameter that serves to measure the compressibility of the elastomer under investigation: it is defined such that in the limit as $\kappa \to +\infty$, the elastomer is incompressible and its stored-energy function reduces to

$$\mathcal{W}(\mathbf{F}) = \begin{cases} W(\mathbf{F}) & \text{if} \quad \det \mathbf{F} = 1 \\ +\infty & \text{otherwise} \end{cases}.$$

An example, to be used in the simulations presented below, is given by the stored-energy function [30]

$$\begin{aligned} \mathcal{W}(\mathbf{F}) = &\sum_{j=1}^{2} \frac{3^{1-b_j}}{2b_j}\mu_j[(\mathbf{F}\cdot\mathbf{F})^{b_j} - 3^{b_j}] - \\ &\sum_{j=1}^{2} \mu_j \ln(\det \mathbf{F}) + \tfrac{\kappa}{2}[\det \mathbf{F} - 1]^2, \end{aligned} \tag{8}$$

where b_j and μ_j $(j = 1, 2)$ are material parameters and where one can readily identify that

$$W(\mathbf{F}) = \sum_{j=1}^{2} \frac{3^{1-b_j}}{2b_j}\mu_j[(\mathbf{F}\cdot\mathbf{F})^{b_j} - 3^{b_j}] - \sum_{j=1}^{2} \mu_j \ln(\det \mathbf{F}),$$

$$g(\mathbf{F}) = \tfrac{1}{2}[\det \mathbf{F} - 1]^2,$$

and that $\kappa = \Lambda + 2\mu/3 - 2(b_1\mu_1 + b_2\mu_2)/3$ in terms of the first and second Lamé constants Λ and $\mu = \mu_1 + \mu_2$ in the limit of small deformations. In the above expressions, the notation $\mathbf{F}\cdot\mathbf{F}$ stands for the square of the Frobenius norm, that is, $\mathbf{F}\cdot\mathbf{F} = F_{ij}F_{ij}$.

The associated parameters η_W and η_κ in (6) stand for small positive numbers that serve to aid the numerical tractability of the vanishingly small stiffness of the regions of the elastomer that have undergone fracture. When dealing with nearly incompressible elastomers, the compressibility parameter κ is typically 10^3 to 10^4 larger than the rest of material parameters describing the elasticity of the elastomer. Thus, to ensure that the fractured regions are indeed of vanishingly small stiffness, and, in particular, "empty" of an elastic fluid, the parameter η_κ needs to be chosen in general much smaller than η_W. For example, in the simulations presented below for a typical nearly incompressible PDMS elastomer, we set $\eta_\kappa = (\mu/\kappa)\eta_W$, where, again, μ stands for the second Lamé constant or initial shear modulus of the elastomer.

Remark 5. *Eqs. (6) and (7) as an approximation of a sharp theory.* Much like in the standard formulation (1), the localization length ε in Eqs. (6) and (7) is just a regularization parameter that is void of any further physical meaning. In principle, accordingly, one should undertake the task of passing to the limit as $\varepsilon \searrow 0$ in the system of Eqs. (6) and (7), showing that it converges to a set of equations that models nucleation and propagation of sharp fracture and healing in elastomers. Although numerical evidence points to the existence of such a set of equations, for now, passing to the limit remains a formidable task because of the technical challenges involved.

Remark 6. *Eqs. (6) and (7) as an Allen–Cahn phase-transition model.* As elaborated in Kumar et al. [24], Eqs. (6) and (7) are in the parlance of phase transitions of Allen–Cahn type, also often referred to as Ginzburg–Landau type; see, e.g., Gurtin [19].

Precisely, Eq. $(6)_1$ stands for the balance of Newtonian forces driving the deformation:

$$\mathrm{Div}\mathbf{S} + \mathbf{b} = \mathbf{0},$$

while Eqs. $(7)_{1-2}$ stand for the balance of configurational forces driving the nucleation and propagation of fracture and healing:

$$\begin{cases} \mathrm{Div}\mathbf{C} + c_i + c_e = (\text{resp. } \geqslant)0, \\ \text{if} \quad 0 < z(\mathbf{X}, t) < 1 \quad \text{and} \quad \dot{z}(\mathbf{X}, t) \neq 0(\text{resp.}=0) \\ \mathrm{Div}\mathbf{C} + c_i + c_e \geqslant (\text{resp. } \leqslant)0, \quad \textit{if} \quad z(\mathbf{X}, t) = 1(\text{resp.}=0) \end{cases}.$$

In the above expressions,

$$\mathbf{S}(\mathbf{X}, t) = (z^2 + \eta_W)\frac{\partial W}{\partial \mathbf{F}}(\nabla \mathbf{y}) + (z^2 + \eta_\kappa)\kappa\frac{\partial g}{\partial \mathbf{F}}(\nabla \mathbf{y})$$

denotes the first Piola–Kirchhoff stress tensor, conjugate to the deformation gradient $\mathbf{F}$, while

$$\begin{cases} c_i(\mathbf{X}, t) = -2z(W(\nabla \mathbf{y}) + \kappa g(\nabla \mathbf{y})) + \frac{3G_c}{8\varepsilon} \\ \mathbf{C}(\mathbf{X}, t) = \frac{3}{4}\varepsilon G_c \nabla z \end{cases}$$

denote the configurational *internal* force c_i and the configurational stress $\mathbf{C}$, conjugate to the configurational variables z and ∇z, at any material point $\mathbf{X} \in \Omega_0$ and time $t \in [0, T]$. In this setting, we also note that the external driving force c_e is referred to as the configurational *external* force.

By the same token, Eqs. (6) and (7) also fall squarely within the realm of governing equations for the so-called non-local generalized standard materials [35]. Two recent contributions that have been derived within that realm for concrete-like materials and that feature an additional driving force of the sort c_e to deal with fracture nucleation are the works of Lorentz [31] and Narayan and Anand [34].

3. Nucleation of fracture in elastomers

At this point, before proceeding with the constitutive prescription of the external driving force $c_e(\mathbf{X}, t)$, it is instructive to recall all the various ways in which fracture can nucleate in elastomers. As established by an abundance of experimental results, macroscopic crack nucleation in homogeneous elastomers — like in any other class of homogeneous elastic brittle materials — falls into one of the three

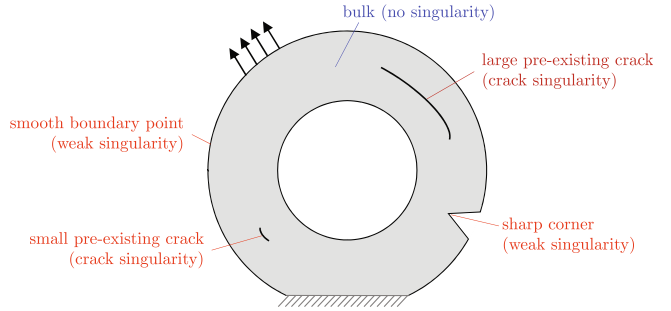

Fig. 1. Schematic of a structure made of a homogeneous elastomer under general quasistatic boundary conditions. Fracture may nucleate: (*i*) at material points in the bulk, (*ii*) from large pre-existing cracks, or (*iii*) from the boundary, be it smooth or sharp, or small pre-existing cracks. Fracture nucleation in the bulk is governed by the strength of the elastomer. On the other hand, fracture nucleation from large pre-existing cracks is governed by the Griffith competition between the material bulk elastic energy and surface fracture energy. Finally, fracture nucleation from the boundary and from small pre-existing cracks is governed by the interaction among all three properties of the elastomer: its strength, its bulk elastic energy, and its surface fracture energy.

different types schematically depicted in Fig. 1: (*i*) nucleation in the bulk, (*ii*) nucleation from large pre-existing cracks, and (*iii*) nucleation from the boundary and small pre-existing cracks. We describe each of these different types in the sequel, one at a time.

Nucleation in the bulk: the strength. Like all materials, elastomers contain inherent defects. These are of possibly different natures, but by and large all of them are submicron in size. When an elastomer is subjected to a state of monotonically increased uniform stress, fracture will nucleate from one or more of those pre-existing defects at a finite critical value of the applied stress. The set of all such critical stresses defines a surface in stress space. In terms of the first Piola–Kirchhoff stress tensor $\mathbf{S}$, we write it

$$\mathcal{F}(\mathbf{S}) = 0. \tag{9}$$

Such a surface is intrinsic, albeit stochastic, and thus a material datum. We refer to it as the *strength surface* of the elastomer.

For the prevalent case of elastomers whose elastic response is isotropic, it is reasonable to postulate that their strength surface is also isotropic. For those elastomers, (9) admits the expedient representations

$$\mathcal{F}(\mathbf{S}) = \widetilde{\mathcal{F}}(s_1, s_2, s_3) = \widehat{\mathcal{F}}(\mathcal{I}_1, \mathcal{I}_2, \mathcal{I}_3) = 0 \tag{10}$$

in terms of the eigenvalues s_1, s_2, s_3 of the Biot stress $\mathbf{S}^{(1)} = (\mathbf{S}^T\mathbf{R} + \mathbf{R}^T\mathbf{S})/2$, $\mathbf{R}$ denoting the rigid rotation stemming from the polar decomposition $\mathbf{F} = \mathbf{R}\mathbf{U}$ of the deformation gradient, and associated principal invariants

$$\begin{aligned} \mathcal{I}_1 &= \mathrm{tr}\,\mathbf{S}^{(1)}, \\ \mathcal{I}_2 &= \tfrac{1}{2}[(\mathrm{tr}\,\mathbf{S}^{(1)})^2 - \mathrm{tr}(\mathbf{S}^{(1)})^2], \\ \mathcal{I}_3 &= \det \mathbf{S}^{(1)}. \end{aligned} \tag{11}$$

In practice, it is difficult to carry out experiments that probe the entire space of uniform stresses in order to measure the entire strength surface (9) or even (10) of a given elastomer of interest. Most of the strength data available in the literature is narrowly restricted to uniaxial tensile strength s_{ts} (when $\mathbf{S} = \mathrm{diag}(s_{\mathrm{ts}}, 0, 0)$ with $s_{\mathrm{ts}} > 0$), hydrostatic tensile strength s_{hs} (when $\mathbf{S} = \mathrm{diag}(s_{\mathrm{hs}}, s_{\mathrm{hs}}, s_{\mathrm{hs}})$ with $s_{\mathrm{hs}} > 0$), and, to a lesser extent, biaxial tensile strength s_{bs} (when $\mathbf{S} = \mathrm{diag}(s_{\mathrm{bs}}, s_{\mathrm{bs}}, 0)$ with $s_{\mathrm{bs}} > 0$); see, e.g., Smith [41], Smith and Rinde [42], Dickie and Smith [8], Gent and Mars [17], and Poulain et al. [37,38].

Remark 7. *Strength surfaces in other stress spaces.* Because of the scarcity of experimental results, it is unclear what measure of stress — whether the first Piola–Kirchhoff stress $\mathbf{S}$, the second Piola–Kirchhoff stress $\mathbf{S}^{(2)} = \mathbf{F}^{-1}\mathbf{S}$, the Cauchy stress $\mathbf{T} = (\det\mathbf{F})^{-1}\mathbf{S}\mathbf{F}^T$, or some other stress measure — is more convenient to describe the strength of elastomers. In this work, we choose the first Piola–Kirchhoff stress $\mathbf{S}$ because it is the stress measure naturally present in the governing Eqs. (6) and (7) and, moreover, it is the easiest to access experimentally.

Nucleation from large pre-existing cracks: the critical energy release. When the domain under investigation contains a large[3] pre-existing crack, fracture may nucleate from the crack front. In other words, the pre-existing crack may propagate. Experimental results have by now settled that the nucleation of fracture from large cracks in elastomers is well described by the Griffith [18] competition between bulk elastic energy and surface fracture energy; see, e.g., Rivlin and Thomas [39] and Extrand and Gent [10]. Roughly speaking, fracture may nucleate from a large pre-existing crack whenever the criterion

$$-\frac{\partial E}{\partial \Gamma} = G_c \tag{12}$$

is satisfied, namely, whenever the change in potential energy E in the structure with respect to an added surface area Γ to the crack reaches the critical elastic energy release rate G_c of the elastomer.

Nucleation from the boundary and small pre-existing cracks: the transition zone. Fracture nucleation from a boundary point, be it smooth or sharp, or a small pre-existing crack in an elastomer is quantitatively less well understood than that taking place in the bulk or from large pre-existing cracks. Qualitatively, nevertheless, it is well established that fracture nucleation from those sites is governed by the mediation between the strength (9) of the elastomer and the Griffith competition (12) between its bulk elastic energy and surface fracture energy.

The three basic material inputs for the modeling of fracture nucleation: $\mathcal{W}(\mathbf{F})$, $\mathcal{F}(\mathbf{S})$, and G_c. Summing up, it is plain from the above that any attempt at a comprehensive macroscopic theory of fracture nucleation in elastomers should account for the stored-energy function $\mathcal{W}(\mathbf{F})$ describing their elasticity, the strength surface $\mathcal{F}(\mathbf{S})$ describing the nucleation of fracture in their bulk, and the critical energy release rate G_c describing nucleation of fracture from the large pre-existing cracks that they may contain. In addition, any such attempt should account for a proper mediation between nucleation in the bulk and from large pre-existing cracks so as to describe properly nucleation of fracture from boundary points and small pre-existing cracks.

The standard phase-field formulation (1) accounts for $\mathcal{W}(\mathbf{F})$ and G_c, but *not* for $\mathcal{F}(\mathbf{S})$. This is why the approach provides a good description of fracture nucleation from large pre-existing cracks, but cannot properly describe when fracture nucleation occurs in the bulk, from boundaries, or from small cracks. To be precise, in the limit as the localization length $\varepsilon \searrow 0$, the formulation (1) predicts critical loads at nucleation from large pre-existing cracks that are at worst only a few tens of a percent larger[4] than the corresponding exact solutions based on the Griffith criterion (12). On the other hand, the formulation (1) incorrectly predicts that the critical applied loads at which fracture nucleates in the bulk, from boundaries, or from small cracks will increase to infinity as the length[5] $\varepsilon \searrow 0$, this for any choice of $\psi(z)$ and $s(z)$.

The presence in the phase-field formulation (6) and (7) of the

[3] "Large" refers to large relative to the characteristic size of the inherent microscopic defects in the elastomer under investigation. By the same token, "small" refers to sizes that are of the same order or just moderately larger than the sizes of the inherent defects.

[4] For a discussion on the use of "damaged notch conditions" along the front of pre-existing cracks as a practical approach to minimize this overshoot, see, e.g., Tanné et al. [44].

[5] Fixing the value of ε to some "physically meaningful" length, as advocated recently in the literature, does not circumvent the problem. Just to mention one issue, fixing the value of ε to match fracture nucleation in the bulk under uniaxial tension according to a given tensile strength s_{ts} (or to any other single strength data point for that matter) would arbitrarily privilege a *single* point on the strength surface while ignoring the rest of that surface; see Section 3.1 in Kumar et al. [25].

stored-energy function $\mathcal{W}(\mathbf{F})$ and the critical energy release rate G_c is directly inherited by construction from the standard phase-field formulation (1). As anticipated in Remark 2 and elaborated in the next section, the strength surface $\mathcal{F}(\mathbf{S})$ enters the formulation (6) and (7) via the external driving force $c_e(\mathbf{X}, t)$. Once the strength surface $\mathcal{F}(\mathbf{S})$ has been accounted for via $c_e(\mathbf{X}, t)$, the phase-field formulation (6) and (7) provides automatically for a proper mediation between the Griffith-dominated and the strength-dominated fracture nucleation regimes. This built-in feature is illustrated by an example in the next section.

4. The constitutive prescription of the external driving force $c_e(\mathbf{X}, t)$ for isotropic elastomers

We are now in a position to delve into the details of how to constitutively prescribe the external driving force $c_e(\mathbf{X}, t)$ in order to incorporate a given strength surface $\mathcal{F}(\mathbf{S})$ into the phase-field formulation (6) and (7). For clarity of exposition, we restrict the presentation to the prominent class of elastomers with overall constitutive isotropy, and within this class, elastomers featuring (with a slight abuse of notation) stored-energy functions of the form[6]

$$\mathcal{W}(\mathbf{F}) = W(I_1, J) + \kappa g(J) \tag{13}$$

and strength surface of the form

$$\mathcal{F}(\mathbf{S}) = \widehat{\mathcal{F}}(\mathcal{I}_1, \mathcal{I}_2) = 0. \tag{14}$$

In relation (13), the arguments I_1 and J stand for the first and the square root of the third principal invariants of the right Cauchy-Green deformation tensor $\mathbf{C} = \mathbf{F}^T\mathbf{F}$, namely,

$$\begin{aligned} I_1 &= \mathrm{tr}\,\mathbf{C}, \\ I_2 &= \tfrac{1}{2}[(\mathrm{tr}\,\mathbf{C})^2 - \mathrm{tr}\,\mathbf{C}^2], \\ I_3 &= \det\mathbf{C} = J^2, \end{aligned} \tag{15}$$

the function $W(I_1, J)$ is taken to satisfy the linearization conditions

$$W(3, 1) = 0, \qquad 2W_{I_1}(3, 1) + W_J(3, 1) = 0,$$

where we have introduced the notation $W_{I_1}(I_1, J) := \partial W(I_1, J)/\partial J$ and $W_J(I_1, J) := \partial W(I_1, J)/\partial J$ for simplicity, and growth condition

$$W(I_1, J) \to C I_1^{p/2} \quad \text{as} \quad ||\mathbf{F}|| \to +\infty \tag{16}$$

for some real exponent $p > 1$ and positive constant C, while the function $g(J)$ is taken to satisfy the linearization conditions

$$g(1) = g'(1) = 0.$$

In this last expression and subsequently, the standard convention $y'(x) = \mathrm{d}y(x)/\mathrm{d}x$ is used to denote the derivative of functions of a single scalar variable.

4.1. The constitutive prescription of Kumar et al. [23] to account for the hydrostatic strength s_{hs}

Prior to introducing the general constitutive prescription for $c_e(\mathbf{X}, t)$ that accounts for the entire strength surface (14), it is appropriate to recall that introduced by Kumar et al. [23], which accounts only for the strength of the elastomer under hydrostatic tensile loading.

Because of their typical near incompressibility, elastomers are prone to fracture within the bulk in regions where the hydrostatic part of the stress is tensile and large while, at the same time, the elastic energy is comparatively small (because the deformation is small). This consistently happens around regions of the elastomer that are bonded to stiff fillers or substrates; see, e.g., the analysis presented by Lefèvre et al. [27] of the classical experiments of Gent and Lindley [15] and Gent and Park [16]. In order to be able to describe nucleation of fracture in those regions, one must therefore account for the hydrostatic tensile strength of the elastomer, that is, for the critical value s_{hs} of the stress s at which fracture nucleates in the elastomer when this is subjected to states of uniform stress of the form $\mathbf{S} = \mathrm{diag}(s, s, s)$ with $s > 0$. To do so, Kumar et al. [23] proposed the following external driving force

$$c_e(\mathbf{X}, t) = -\beta^\varepsilon z \frac{3^{p/2}}{I_1^{p/2}} \kappa g'(J). \tag{17}$$

Here, the term $\kappa g'(J)$ corresponds to the hydrostatic part $(1/3)\mathrm{tr}\mathbf{T}$ of the Cauchy stress $\mathbf{T} = J^{-1}\mathbf{S}\mathbf{F}^T$ associated with the compressibility parameter κ, where $\mathbf{S} = \partial\mathcal{W}(\mathbf{F})/\partial\mathbf{F}$. The preceding quotient is a normalized measure of stretch, which takes the value of 1 in the absence of stretch when $\mathbf{F} \in Orth^+$. For large stretches, the quotient — and hence the force c_e — approaches zero with the inverse of the norm $I_1^{p/2}$, which controls the growth (16) of the elastic energy at large stretches. The dimensionless coefficient β^ε is given by the formula (see the Appendix in [23])

$$\beta^\varepsilon = \frac{\lambda_{\mathrm{hs}}^p}{\kappa g'(\lambda_{\mathrm{hs}}^3)}\left[\frac{3G_c}{8\varepsilon} - 2W(3\lambda_{\mathrm{hs}}^2, \lambda_{\mathrm{hs}}^3) - 2\kappa g(\lambda_{\mathrm{hs}}^3)\right] \tag{18}$$

with λ_{hs} defined implicitly as the smallest root larger than 1 of the nonlinear algebraic equation

$$s_{\mathrm{hs}} = 2\lambda_{\mathrm{hs}} W_{I_1}(3\lambda_{\mathrm{hs}}^2, \lambda_{\mathrm{hs}}^3) + \lambda_{\mathrm{hs}}^2 W_J(3\lambda_{\mathrm{hs}}^2, \lambda_{\mathrm{hs}}^3) + \kappa\lambda_{\mathrm{hs}}^2 g'(\lambda_{\mathrm{hs}}^3), \tag{19}$$

where, again, s_{hs} stands for the hydrostatic tensile strength of the given elastomer.

Remark 8. *The case of nearly incompressible elastomers.* In the limit of incompressibility as $\kappa \to +\infty$, the nonlinear algebraic Eq. (19) admits the explicit asymptotic solution

$$\lambda_{\mathrm{hs}} = 1 + \frac{s_{\mathrm{hs}}}{3\kappa g''(1)} + O\left(\frac{1}{\kappa^2}\right).$$

In turn, the expression (18) for the coefficient β^ε reduces to leading order to the fully explicit expression

$$\beta^\varepsilon = \frac{3G_c}{8 s_{\mathrm{hs}}\varepsilon}.$$

Remark 9. *Stochasticity of the hydrostatic strength s_{hs}.* The value of the hydrostatic strength s_{hs} is not expected to be constant throughout the domain Ω_0 occupied by the elastomer but, instead, to take spatially random heterogeneous values in some range $[s_{\mathrm{hs}}^{min}, s_{\mathrm{hs}}^{max}]$. This is because the strength at a macroscopic material point $\mathbf{X}$ depends on the nature of the underlying microscopic defects from which fracture initiates, and this is known to exhibit a stochastic spatial variation in any given piece of elastomer; see, e.g., Gent [13].

Remark 10. *Predictive capabilities.* The direct comparisons reported by Kumar et al. [23],[24] with the experiments of Poulain et al. [37,38] on three different types of PDMS elastomers have shown that the external driving force (17) renders a phase-field model (6) and (7) capable of accurately predicting fracture nucleation at material points in the bulk that are subject to a purely hydrostatic stress.

[6] We emphasize that the development presented in this section applies *mutatis mutandis* to any isotropic stored-energy function of choice. Our restriction to stored-energy functions of the form (13) is based purely on clarity of presentation. From an applications point of view, we also emphasize, however, that stored-energy functions of the form (13) include many models — such as the Neo-Hookean [45], Arruda and Boyce [3], Gent [14], and Lopez-Pamies [30] models — which have been shown to describe reasonably well the response of a broad variety of elastomers.

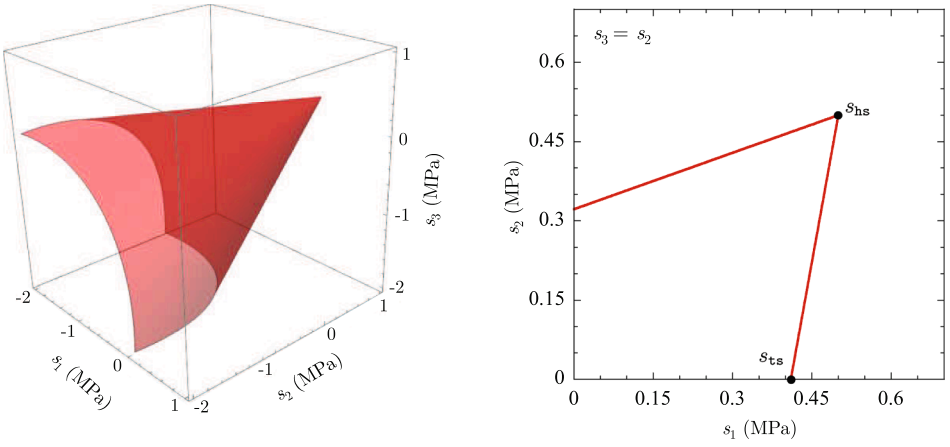

Fig. 2. Strength surface (20) with material parameters (21) for $s_{ts} = 0.41$ MPa and $s_{hs} = 0.50$ MPa, which are representative of a PDMS elastomer. (a) Plot of the entire surface in the space of principal stresses (s_1, s_2, s_3). (b) Plot of the surface in the space of principal stresses (s_1, s_2) with $s_3 = s_2$.

4.2. A constitutive prescription that accounts for the entire strength surface $\widehat{\mathcal{F}}(\mathcal{I}_1, \mathcal{I}_2)$

We now turn to the new constitutive prescription for the external driving force $c_e(\mathbf{X}, t)$ that generalizes (17) to account for the entire strength surface (14) of the elastomer.

As alluded to earlier, the strength surface (14) of a given elastomer of interest is at best only known at a few select points in stress space. Mostly, only the uniaxial tensile strength s_{ts} and the hydrostatic tensile strength s_{hs} may be freely available in the literature. So in practice one must resort to the use of a model to extrapolate the available strength data to the entire stress space.

In the sequel, for definiteness, we present a constitutive prescription for the external driving force $c_e(\mathbf{X}, t)$ for the case when the given strength surface (14) is of the Drucker-Prager type

$$\widehat{\mathcal{F}}(\mathcal{I}_1, \mathcal{I}_2) = \sqrt{\frac{\mathcal{I}_1^2}{3} - \mathcal{I}_2} + \gamma_1 \mathcal{I}_1 + \gamma_0 = 0, \tag{20}$$

where γ_0 and γ_1 stand for material parameters; in their original work, Drucker and Prager [9] proposed a surface of the form (20) to model the yielding of soils. When the material parameters γ_0 and γ_1 are calibrated with the uniaxial tensile and hydrostatic tensile strengths, they read as

$$\gamma_0 = -\frac{\sqrt{3}\, s_{hs} s_{ts}}{3 s_{hs} - s_{ts}} \quad \text{and} \quad \gamma_1 = \frac{s_{ts}}{\sqrt{3}\,(3 s_{hs} - s_{ts})}. \tag{21}$$

By way of an example, Fig. 2 presents plots of the strength surface (20) with material parameters (21) for the values $s_{ts} = 0.41$ MPa and $s_{hs} = 0.50$ MPa, which are representative of one of the six different types of PDMS Sylgard 184 elastomers[7] investigated by Poulain et al. [37,38], specifically, the one labeled PDMS 30:1. Fig. 2(a) shows the entire strength surface in the space of principal stresses (s_1, s_2, s_3). Fig. 2(b) shows the strength surface in the projected space (s_1, s_2) with $s_3 = s_2$ and singles out the values of the uniaxial tensile strength s_{ts} and the hydrostatic tensile strength s_{hs}.

Now, in a companion contribution, Kumar et al. [25] have provided a road map that allows one to construct an external driving force $c_e(\mathbf{X}, t)$ for any given strength surface in the basic context of linear elastic brittle materials. Roughly speaking, the idea is to choose an external driving force that:

- has identical functional form as the given strength surface but whose coefficients are ε-dependent and suitably selected so that, in the limit as the localization length $\varepsilon \searrow 0$, the resulting phase-field model (6) and (7) predicts fracture nucleation in the bulk exactly according to the given strength surface, and
- features a suitably selected prefactor that makes the force vanish at crack fronts so that the resulting phase-field model (6) and (7) predicts a propagation of fracture that is undisturbed by the presence of such a force and hence remains governed by the critical energy release rate G_c.

The same two-pronged idea applies *mutatis mutandis* to the hyperelastic brittle materials of interest here. Accordingly, following Kumar et al. [25], a constitutive prescription for $c_e(\mathbf{X}, t)$ that accounts for the strength surface (20) is given by

$$c_e(\mathbf{X}, t) = \hat{c}_e(\mathcal{I}_1, \mathcal{I}_2; \varepsilon) = \frac{1}{1 + \beta_3^\varepsilon \mathcal{I}_1^2}\left(\beta_2^\varepsilon \sqrt{\frac{\mathcal{I}_1^2}{3} - \mathcal{I}_2} + \beta_1^\varepsilon \mathcal{I}_1 + \beta_0^\varepsilon\right), \tag{22}$$

where $\mathcal{I}_1$ and $\mathcal{I}_2$ are the principal invariants $(11)_{1,2}$ of the Biot stress tensor associated with the given stored-energy function (13) and the degradation function $(2)_1$, namely,

$$\mathbf{S}^{(1)} = z^2 [2 W_{I_1}(I_1, J)\mathbf{U} + J W_J(I_1, J)\mathbf{U}^{-1} + \kappa J g'(J)\mathbf{U}^{-1}], \tag{23}$$

and where the coefficients β_0^ε, β_1^ε, β_2^ε, and β_3^ε are given by

$$\begin{aligned}
\beta_0^\varepsilon &= \left(\frac{\alpha^\varepsilon \mu}{s_{ts}}\right)\frac{3G_c}{8\varepsilon},\\
\beta_1^\varepsilon &= -\left(\frac{\alpha^\varepsilon \mu + s_{ts}}{3 s_{ts} s_{hs}}\right)\frac{3G_c}{8\varepsilon} + \frac{2\mathcal{W}_{hs}}{3 s_{hs}} - \frac{9 s_{ts} s_{hs}}{8\mu\kappa} + \left(\frac{6 s_{ts} s_{hs} \mathcal{W}_{hs}}{\mu\kappa}\right)\frac{\varepsilon}{G_c},\\
\beta_2^\varepsilon &= -\left(\frac{(\alpha^\varepsilon \mu + s_{ts})(3 s_{hs} - s_{ts})}{\sqrt{3}\, s_{hs} s_{ts}^2}\right)\frac{3G_c}{8\varepsilon} + \frac{3\sqrt{3}\,(3 s_{hs} - s_{ts}) s_{ts}}{8\mu\kappa} + \frac{6 s_{hs} \mathcal{W}_{ts} - 2 s_{ts} \mathcal{W}_{hs}}{\sqrt{3}\, s_{hs} s_{ts}} +\\
&\quad \left(\frac{2\sqrt{3}\, s_{ts}(s_{ts} \mathcal{W}_{ts} - 3 s_{hs} \mathcal{W}_{hs})}{\mu\kappa}\right)\frac{\varepsilon}{G_c},\\
\beta_3^\varepsilon &= \left(\frac{s_{ts}}{\mu\kappa}\right)\frac{\varepsilon}{G_c}.
\end{aligned} \tag{24}$$

In these last expressions, α^ε is an ε-dependent coefficient whose selection is described further below while $\mathcal{W}_{ts}$ and $\mathcal{W}_{hs}$ stand for the values of the stored-energy function (13) along uniaxial and hydrostatic tensile uniform stress states at which fracture nucleates in the given elastomer. Precisely,

[7] It is worth noting here that PDMS Sylgard 184 elastomers, supplied by Dow Corning, have long been utilized in a variety of research and practical contexts; see, e.g., Gent and Park [16], Johnston et al. [22], Milner et al. [33], and Leonard et al. [28].

$$\mathcal{W}_{\rm ts} = W(\lambda_{\rm ts}^2 + 2\lambda_l^2, \lambda_{\rm ts}\lambda_l^2) + \kappa g(\lambda_{\rm ts}\lambda_l^2),$$
$$\mathcal{W}_{\rm hs} = W(3\lambda_{\rm hs}^2, \lambda_{\rm hs}^3) + \kappa g(\lambda_{\rm hs}^3),$$

where the pair of stretches $(\lambda_{\rm ts},\ \lambda_l)$ and the stretch $\lambda_{\rm hs}$ are defined implicitly as the roots closest to (1,1) and 1 of the systems of nonlinear algebraic equations

$$\begin{cases} s_{\rm ts} = 2\lambda_{\rm ts} W_{I_1}(\lambda_{\rm ts}^2 + 2\lambda_l^2, \lambda_{\rm ts}\lambda_l^2) + \lambda_l^2 W_J(\lambda_{\rm ts}^2 + 2\lambda_l^2, \lambda_{\rm ts}\lambda_l^2) + \kappa\lambda_l^2 g'(\lambda_{\rm ts}\lambda_l^2) \\ 0 = 2\lambda_l W_{I_1}(\lambda_{\rm ts}^2 + 2\lambda_l^2, \lambda_{\rm ts}\lambda_l^2) + \lambda_{\rm ts}\lambda_l W_J(\lambda_{\rm ts}^2 + 2\lambda_l^2, \lambda_{\rm ts}\lambda_l^2) \\ \qquad + \kappa\lambda_{\rm ts}\lambda_l g'(\lambda_{\rm ts}\lambda_l^2) \end{cases} \tag{25}$$

and

$$s_{\rm hs} = 2\lambda_{\rm hs} W_{I_1}(3\lambda_{\rm hs}^2, \lambda_{\rm hs}^3) + \lambda_{\rm hs}^2 W_J(3\lambda_{\rm hs}^2, \lambda_{\rm hs}^3) + \kappa\lambda_{\rm hs}^2 g'(\lambda_{\rm hs}^3), \tag{26}$$

respectively.

Remark 11. *Explicit dependence on the deformation field* $\mathbf{y}(\mathbf{X}, t)$ *and the phase field* $z(\mathbf{X}, t)$. A straightforward calculation shows that the invariants $(11)_{1,2}$ of the Biot stress (23) entering the constitutive prescription (22) for the external driving force $c_{\rm e}(\mathbf{X}, t)$ can be compactly written as

$$\mathcal{I}_1 = 2z^2 i_1 W_{I_1}(I_1, J) + z^2 i_2 (W_J(I_1, J) + \kappa g'(J))$$

and

$$\mathcal{I}_2 = 4z^4 i_2 W_{I_1}^2(I_1, J) + z^4 i_1 J (W_J(I_1, J) + \kappa g'(J))^2 + 2z^4 (i_1 i_2 - 3J)(W_J(I_1, J) + \kappa g'(J)) W_{I_1}(I_1, J)$$

in terms of the principal invariants (15) of the right Cauchy-Green deformation tensor $\mathbf{C}$ and of the first and second principal invariants of the right stretch tensor $\mathbf{U}$:

$$i_1 = {\rm tr}\,\mathbf{U} \qquad \text{and} \qquad i_2 = \frac{1}{2}[({\rm tr}\,\mathbf{U})^2 - {\rm tr}\,\mathbf{U}^2]. \tag{27}$$

Recalling that the invariants (27) of $\mathbf{U}$ can be written explicitly in terms of the invariants (15) of $\mathbf{C}$ permits to circumvent having to carry out (numerically) the polar decomposition of the deformation gradient tensor $\mathbf{F}$ and, in turn, to write explicitly the dependence of the external driving force (22) on the deformation field $\mathbf{y}(\mathbf{X}, t)$. Note that the dependence of (22) on the phase field $z(\mathbf{X}, t)$ is explicit as well. For completeness, we report here the explicit connections between $i_1,\ i_2$ and $I_1,\ I_2,\ J$:

$$\begin{cases} i_1 = \begin{cases} \frac{1}{2}\left(\sqrt{2I_1 + \xi_3} + \sqrt{2I_1 - \xi_3 + \frac{16J}{\sqrt{2I_1 + \xi_3}}}\right) & \text{if} \quad \xi_3 \neq -2I_1 \\ \sqrt{I_1 + 2\sqrt{I_2}} & \text{if} \quad \xi_3 = -2I_1 \end{cases} \\ i_2 = \sqrt{I_2 + 2i_1 J} \end{cases}, \tag{28}$$

where

$$\xi_3 = -\frac{2}{3}I_1 + (\xi_1 + \sqrt{\xi_2})^{1/3} + (\xi_1 - \sqrt{\xi_2})^{1/3}$$

with

$$\xi_1 = \tfrac{2^5}{27}(2I_1^3 - 9I_1 I_2 + 27J^2) \quad \text{and}$$
$$\xi_2 = \tfrac{2^{10}}{27}(4I_2^3 - I_1^2 I_2^2 + 4I_1^3 J^2 - 18 I_1 I_2 J^2 + 27J^4);$$

see Hoger and Carlson [20] and Steigmann [43].

Remark 12. *The material inputs entering the external driving force (22).* The external driving force (22) with coefficients (24) depends on the stored-energy function (13) describing the elasticity of the elastomer via the parameters $\mu,\ \kappa,\ \mathcal{W}_{\rm ts},\ \mathcal{W}_{\rm hs}$, on the material parameters $s_{\rm ts},\ s_{\rm hs}$ describing its strength surface (20), as well as on its critical energy release rate G_c. It is *fully explicit* up to the evaluation of the quantities $\mathcal{W}_{\rm ts},\ \mathcal{W}_{\rm hs}$, which requires the numerical solution of the nonlinear algebraic Eqs. (25), (26), and the prescription of the coefficient α^ε, which is described in Section 4.2.2 below.

4.2.1. Nucleation in the bulk

Under states of uniform stress $\mathbf{S}$, the phase-field model (6) and (7) with external driving force (22) and coefficients (24) predicts that the phase field z ceases to be identically 1 and localizes near 0 whenever the algebraic equation[8]

$$\mathcal{F}^\varepsilon(\mathcal{I}_1, \mathcal{I}_2, \mathcal{I}_3) = 2W(I_1, J) + 2\kappa g(J) - \hat{c}_{\rm e}(\mathcal{I}_1, \mathcal{I}_2; \varepsilon) - \frac{3G_c}{8\varepsilon} = 0 \tag{29}$$

is satisfied, where $\mathcal{I}_1, \mathcal{I}_2, \mathcal{I}_3$ stand for the invariants (11) of the Biot stress $\mathbf{S}^{(1)}$ associated with the applied uniform first Piola–Kirchhoff stress $\mathbf{S}$ and where the arguments I_1 and J in the energetic terms W and g are given in terms of these stress invariants by the implicit relations

$$\begin{cases} 2i_1 W_{I_1}(I_1, J) + i_2(W_J(I_1, J) + \kappa g'(J)) = \mathcal{I}_1, \\ 4i_2 W_{I_1}^2(I_1, J) + i_1 J(W_J(I_1, J) + \kappa g'(J))^2 + 2(i_1 i_2 - 3J)(W_J(I_1, J) + \kappa g'(J)) W_{I_1}(I_1, J) = \mathcal{I}_2, \\ 8JW_{I_1}^3(I_1, J) + J^2(W_J(I_1, J) + \kappa g'(J))^3 + 4(i_2^2 - 2i_1)(W_J(I_1, J) + \kappa g'(J)) W_{I_1}^2(I_1, J) + \\ 2(i_1^2 - 2i_2) J(W_J(I_1, J) + \kappa g'(J))^2 W_{I_1}(I_1, J) = \mathcal{I}_3; \end{cases} \tag{30}$$

recall that the invariants i_1 and i_2 are given in terms of I_1, I_2, and J by expressions (28). *Id est*, Eq. (29) defines the strength surface — in the space of first Piola–Kirchhoff stresses — predicted by the phase-field model. In the limit as the localization length $\varepsilon \searrow 0$, assuming rather generally that the asymptotic behavior of the coefficient α^ε is taken to be of the form $\alpha^\varepsilon = \alpha_0\varepsilon^{-r} + \alpha_1\varepsilon^{-r+1} + \alpha_2\varepsilon^{-r+2} + \ldots$ for some $r > 0$, it is a simple matter to establish that Eq. (29) reduces asymptotically to

$$\mathcal{F}^\varepsilon(\mathcal{I}_1, \mathcal{I}_2, \mathcal{I}_3) = -\frac{3\alpha_0\mu G_c}{8 s_{\rm ts}\gamma_0\varepsilon^{1+r}}\left(\sqrt{\frac{\mathcal{I}_1^2}{3} - \mathcal{I}_2} + \gamma_1\mathcal{I}_1 + \gamma_0\right) = 0$$

to leading order, where we recall that the material parameters γ_0, γ_1 are given by expressions (21). *Id est*, the strength surface (29) predicted by the phase-field model (6) and (7) with external driving force (22) and coefficients (24) *agrees identically* with the given strength surface (20) of the elastomer in the limit as $\varepsilon \searrow 0$, this for any choice of the coefficient α^ε with the asymptotic behavior indicated above. For finite values of ε, moreover, the strength surface (29) predicted by the phase-field model provides an approximation for the given strength surface (20) that — by construction — has the merit to agree identically with it along uniaxial and hydrostatic tension, namely, when $\mathcal{I}_1 = s_{\rm ts},\ \mathcal{I}_2 = \mathcal{I}_3 = 0$ and $\mathcal{I}_1 = 3s_{\rm hs},\ \mathcal{I}_2 = 3s_{\rm hs}^2,\ \mathcal{I}_3 = s_{\rm hs}^3$, respectively. This agreement is possible for *any* value of the coefficient α^ε and *any* value of the localization length ε thanks to the choice of corrections of $O(1)$ and $O(\varepsilon)$ in the expressions $(24)_{2-3}$ for the coefficients β_1^ε and β_2^ε.

Remark 13. *The case of nearly incompressible elastomers.* In the limit of incompressibility as $\kappa \to +\infty$, it is straightforward to show that the implicit relations (30) reduce asymptotically to the partially explicit expressions

[8] Note that condition (29) is nothing more than the right-hand side of the evolution Eq. $(7)_1$ for the phase field z evaluated at $z = 1$ with $\dot{z} < 0$ and set to zero. For a discussion of its physical meaning as a stability condition, we refer the interested reader to Appendix B in Kumar et al. [25].

$$\begin{cases} J = 1 + O\left(\frac{1}{\kappa}\right), \\ \frac{i_1}{i_2^2}\mathcal{I}_1^2 + \frac{2(-2i_1^2 - 3i_2 + i_1 i_2^2)}{i_2^2}\mathcal{I}_1 W_{I_1}(I_1, 1) + \frac{4(i_1^3 + 3i_1 i_2 - i_1^2 i_2^2 + i_2^3)}{i_2^2} W_{I_1}^2(I_1, 1) + O\left(\frac{1}{\kappa}\right) = \mathcal{I}_2, \\ \frac{\mathcal{I}_1^3}{i_2^3} - \frac{2(3i_1 - i_1^2 i_2 + 2i_2^2)}{i_2^3}\mathcal{I}_1^2 W_{I_1}(I_1, 1) + \frac{4(3i_1^2 - 2i_1^3 i_2 + 2i_1 i_2^2 + i_2^4)}{i_2^3}\mathcal{I}_1 W_{I_1}^2(I_1, 1) + \\ \frac{8(-i_1^3 + i_1^4 i_2 + i_2^3 - i_1 i_2^4)}{i_2^3} W_{I_1}^3(I_1, 1) + O\left(\frac{1}{\kappa}\right) = \mathcal{I}_3, \end{cases} \tag{31}$$

and, in turn, that the strength surface (29) predicted by the phase-field model reduces to

$$\mathcal{F}^\varepsilon(\mathcal{I}_1, \mathcal{I}_2, \mathcal{I}_3) = 2W(I_1, 1) - \hat{c}_e(\mathcal{I}_1, \mathcal{I}_2; \varepsilon) - \frac{3G_c}{8\varepsilon} = 0$$

to leading order, where the argument I_1 in the energetic term W is given now in terms of the stress invariants $\mathcal{I}_1$, $\mathcal{I}_2$, $\mathcal{I}_3$ by the implicit relations $(31)_{2,3}$.

Remark 14. *Stochasticity of the strength material parameters s_{ts} and s_{hs}.* As already pointed out in Remark 9 in the context of the basic external driving force (17), the values of the strength material parameters $s_{\rm ts}$ and $s_{\rm hs}$ in the external driving force (22) with (24) are not expected to be constant throughout the domain Ω_0 occupied by the elastomer, but to take spatially random heterogeneous values in some ranges $[s_{\rm ts}^{min}, s_{\rm ts}^{max}]$ and $[s_{\rm hs}^{min}, s_{\rm hs}^{max}]$. Once more, this is because the strength at a macroscopic material point $\mathbf{X}$ depends on the specifics of the underlying microscopic defects from which fracture initiates, and these exhibit a stochastic spatial variation in any given piece of elastomer.

4.2.2. Nucleation from large pre-existing cracks: The selection of the coefficient α^ε

The preceding subsection has established that the phase-field model (6) and (7) with external driving force (22) and coefficients (24) predicts fracture nucleation in the bulk according to the strength surface (20) of the given elastomer, this for any choice (within a very large class) of the coefficient α^ε. It turns out, however, that the value of α^ε *does* affect when the phase-field model predicts nucleation from large pre-existing cracks and hence must be calibrated accordingly.

In order to determine the correct value of α^ε for a given set of material function $W(I_1, J) + \kappa g(J)$ and parameters $s_{\rm ts}$, $s_{\rm hs}$, G_c and a given localization length ε, one must consider and solve a boundary-value problem for which the nucleation from a large pre-existing crack is determined first according to the Griffith criterion (12) and then have the phase-field model (6) and (7) with external driving force (22) and coefficients (24) match that solution thereby determining α^ε.

Among plenty of possible boundary-value problems to choose from, because of its computational and experimental accessibility, one natural candidate is the so-called "pure shear" test introduced by Rivlin and Thomas [39]. As schematically illustrated by Fig. 3(b), the specimen in this test consists of an elastomer sheet of initial height l_0 and much larger width w_0 that contains a large pre-existing crack, of length a say, on one of its sides along its centerline. The sheet is clamped on its top and bottom and subject to a prescribed displacement u. It is indeed a simple matter to solve this problem numerically[9] — for instance, via finite elements — to determine the critical value u_{cr} of the applied displacement u at which the crack will propagate according to the Griffith criterion (12). It is equally straightforward to carry out the corresponding experiment with conventional equipment.

For demonstration purposes and later use in the simulations presented in Section 5, Fig. 3(a) reports the computed value of the coefficient α^ε for which the phase-field model (6) and (7), with external driving force (22) and coefficients (24), predicts the same critical displacement u_{cr} as the Griffith criterion (12) at which the crack propagates in the "pure shear" test of a PDMS elastomer. Specifically, the results are presented as a function of the localization length ε and correspond to computations for a specimen with initial height $l_0 = 10$ mm, width $w_0 = 50$ mm, and crack length $a = 10$ mm made of a 2-mm-thick sheet of elastomer featuring stored-energy function (8) with elastic material parameters $\mu_1 = 0.03192$ MPa, $b_1 = 1.39107$, $\mu_2 = 0.01857$ MPa, $b_2 = -1.02103$, $\kappa = 10^3(\mu_1 + \mu_2) = 50.49$ MPa, strength material parameters $s_{\rm ts} = 0.41$ MPa, $s_{\rm hs} = 0.50$ MPa, and critical energy release rates $G_c = 20$ J/m^2 and $k_{\mathcal{H}} = 0$, material properties which are representative of the PDMS 30:1 elastomer investigated by Poulain et al. [37,38]. For completeness, we summarize in the Appendix the calibration process behind the above-listed material parameters for the PDMS 30:1 elastomer.

We close this subsection by emphasizing that the value of α^ε obtained in the above-outlined procedure is independent of the size and type of boundary-value problem chosen to match the prediction from the phase-field model with that of the Griffith criterion. In other words, the coefficient α^ε can be thought of as an ε-dependent material parameter.

Remark 15. *Stochasticity of the coefficient α^ε.* When calibrated for strength material parameters $s_{\rm ts}$ and $s_{\rm hs}$ taking stochastic values in some ranges $[s_{\rm ts}^{min}, s_{\rm ts}^{max}]$ and $[s_{\rm hs}^{min}, s_{\rm hs}^{max}]$, the coefficient α^ε will not be constant but, instead, will inherent some of the stochasticity of the strength material parameters. Numerical tests suggest, however, that the use of a constant value of α^ε fitted to the average strength surface suffices for all practical purposes (so long as none of the ranges $[s_{\rm ts}^{min}, s_{\rm ts}^{max}]$, $[s_{\rm hs}^{min}, s_{\rm hs}^{max}]$ is exceedingly large).

4.2.3. Nucleation from the boundary and small pre-existing cracks

The two preceding subsections have established that the phase-field model (6) and (7) with external driving force (22) and coefficients (24), granted the appropriate calibration of α^ε, predicts fracture nucleation in the bulk according to the strength surface (20) and from large pre-existing cracks according to the Griffith competition between bulk elastic energy and surface fracture energy (12), as desired. As remarked at the conclusion of Section 3, such a phase-field model provides automatically for a proper mediation between fracture nucleation in the bulk and from large pre-existing cracks and is thus able to describe fracture nucleation from boundary points and small pre-existing cracks without any further calibration. We illustrate this built-in property by means of an example.

For possible comparison with experiments, we consider the problem of a 1-mm-thick sheet of the same PDMS elastomer considered in Fig. 3, with 15 mm initial height and 5 mm initial width embedding a crack on one of its sides along its centerline, that is clamped on its top and bottom and subject to a prescribed displacement u; see Fig. 4(a) for a schematic. Fig. 4(b) reports the critical stress s_{cr} predicted by the phase-field model at which the crack starts propagating in such a test; in terms of the critical value P_{cr} of the force P predicted by the model, the stress is given by $s_{cr} = P_{cr}/(1\,\text{mm} \times 5\,\text{mm})$. The results are plotted as a function of the size a of the crack for three decreasing values of the localization length, $\varepsilon = 3.5$, 2.0, and 0.5 μm. The corresponding values of the coefficient α^ε can be read off Fig. 3(a). They are $\alpha^\varepsilon = 1933$, 108, and -0.95, respectively.

Two main observations are clear from Fig. 4. First, the proposed phase-field model captures correctly — at least in a qualitative sense — the transition from the strength-dominated fracture ($\widehat{\mathcal{F}}(\mathcal{I}_1, \mathcal{I}_2) = 0$) to the critical-energy-release-rate-dominated fracture ($-\partial E/\partial\Gamma = G_c$). Indeed, the results show that fracture nucleation from pre-existing cracks that are smaller than some threshold size, in this case roughly $a = 1.5$

[9] For the case of incompressible elastomers, Rivlin and Thomas [39] provided an approximate formula for u_{cr}, which is very simple, albeit implicit, and happens to be independent of the length a of the pre-existing crack. In the present notation, their formula reads $W(\lambda_{cr}^2 + \lambda_{cr}^{-2} + 1, 1)l_0 = G_c$ with $\lambda_{cr} = 1 + u_{cr}/l_0$.

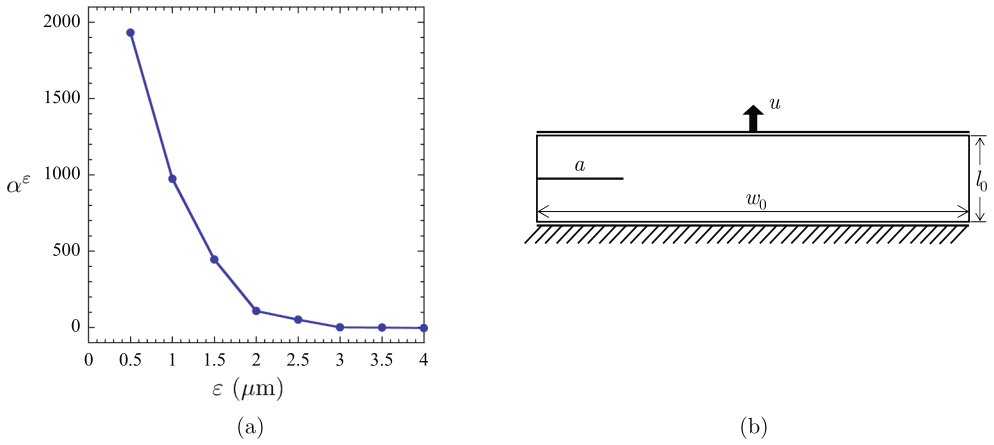

Fig. 3. (a) The value of the coefficient α^ε for a PDMS elastomer, plotted as a function of the localization length ε and determined by matching the prediction of the phase-field model (6) and (7), with external driving force (22) and coefficients (24), with that of the Griffith criterion (12) for the critical displacement u_{cr} at which the pre-existing crack in the "pure shear" test schematically depicted in (b) starts propagating.

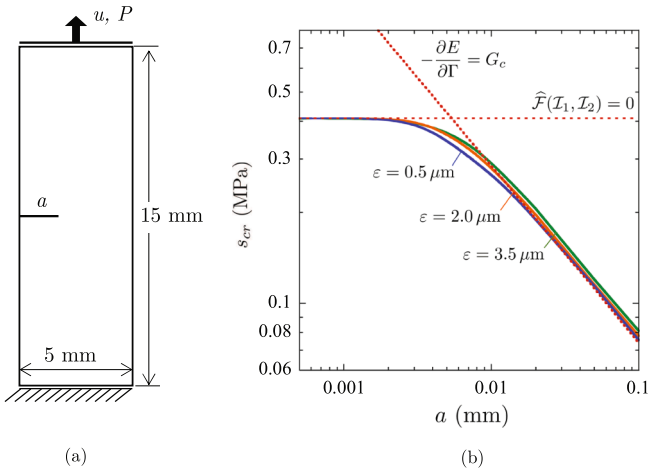

Fig. 4. (a) Schematic of the boundary-value problem (thickness 1 mm) used to illustrate the built-in capability of the phase-field model (6) and (7), with external driving force (22) and coefficients (24), to describe fracture nucleation from a small pre-existing crack. (b) The critical stress s_{cr} predicted by the phase-field model, for three decreasing values of the localization length ε, at which the pre-existing crack starts propagating in the boundary-value problem depicted in (a). The results are plotted as a function of the size a of the crack and pertain to the same PDMS elastomer considered in Fig. 3. For direct comparison, the limiting results for fracture nucleation occurring based on the strength criterion ($\widehat{\mathcal{F}}(\mathcal{I}_1, \mathcal{I}_2) = 0$) and on the critical energy release rate criterion ($-\partial E/\partial\Gamma = G_c$) are also included.

μm, is governed by the strength of the elastomer, while fracture nucleation from pre-existing cracks that are larger than some other threshold size, in this case roughly $a = 25$ μm, is governed by the critical energy release rate of the elastomer. Fracture nucleation from pre-existing cracks featuring sizes between those thresholds is governed by some interpolation, in accordance with experimental observations.

The second main observation from Fig. 4 is that the phase-field solutions for different values of the localization length ε are qualitatively very similar to one another and seem to converge as ε decreases.

4.2.4. Crack propagation

The three preceding subsections have established that the presence of the external driving force (22), with coefficients (24) and a properly calibrated value of α^ε, in the governing Eqs. (6) and (7) renders a phase-field model capable of modeling nucleation of fracture in the bulk, from large pre-existing cracks, as well as from boundary points and small pre-existing cracks in isotropic elastomers undergoing arbitrarily large quasistatic deformations. In this final subsection, we show that the presence of such an external driving force does not interfere with the propagation of fracture in the sense that the proposed phase-field model (6) and (7) predicts the same crack propagation as the standard phase-field model (1), and hence the same crack propagation as that dictated by the Griffith competition between bulk elastic energy and surface fracture energy. We do so by means of an example.

A convenient boundary-value problem to investigate how a given phase-field model describes the propagation of cracks is the "surfing" boundary-value problem introduced by Hossain et al. [21] in the context of linear elastic materials. The basic idea consists in subjecting a long strip of the material of interest with a pre-existing crack on its side to a suitably selected deformation boundary condition that makes the pre-existing crack propagate at a prescribed "velocity" V. Consider hence the 0.02-mm-thick strip of elastomer schematically depicted in Fig. 5(a), with 0.5 mm initial width and 0.1 mm initial height, embedding an edge crack of initial length $a = 0.05$ mm along its centerline in the $\mathbf{e}_1$ direction. In order to make the crack propagate at a prescribed "velocity" V, we subject the top ($X_2 = 0.05$ mm) and bottom ($X_2 = -0.05$ mm) boundaries of the strip to a deformation of the form

$$\bar{y}_2(\mathbf{X}, t) = X_2 + \bar{u}_2(\mathbf{X}, t) \quad \text{with}$$
$$\bar{u}_2(\mathbf{X}, t) = \begin{cases} t\,\bar{u}(X_1 - Vt^*, X_2) & \text{if} \quad 0 \leqslant t \leqslant t^* \\ t^*\bar{u}(X_1 - Vt, X_2) & \text{if} \quad t > t^* \end{cases}. \tag{32}$$

That is, from the initial time $t = 0$ up to t^*, the deformation is ramped up to the point at which there is nearly enough elastic energy in the strip for the pre-existing crack to start propagating. For times $t > t^*$, the applied deformation is then simply "translated" along the $\mathbf{e}_1$ direction with the "velocity" V. The particular form of the function $\bar{u}$ in (32) is not critically important. Here, for definiteness, we make use of

$$\bar{u}(X_1 - Vt, X_2) = \frac{A}{2}\left(1 - \tanh\left(\frac{X_1 - Vt}{d}\right)\right)\mathrm{sgn}(X_2), \tag{33}$$

where A and d are constants, which is one of the forms utilized by Hossain et al. [21].

Fig. 5 shows results for the crack propagation in the strip as predicted by the proposed phase-field model for the choice of parameters $V = 0.2$ mm, $t^* = 1.0$, $A = 0.15$ mm, $d = 0.05$ mm in the applied deformation (32) with (33). The results pertain to the same PDMS elastomer considered above and the same three decreasing values of the localization length $\varepsilon = 3.5$, 2.0, and 0.5 μm considered in Fig. 4. Specifically, Fig. 5(c) reports the evolution of the energy release rate G in the strip, obtained by calculating the J-integral over the boundary of the strip, while Fig. 5(d) shows the associated crack length a, both as functions of the time t parameterizing the applied load. For

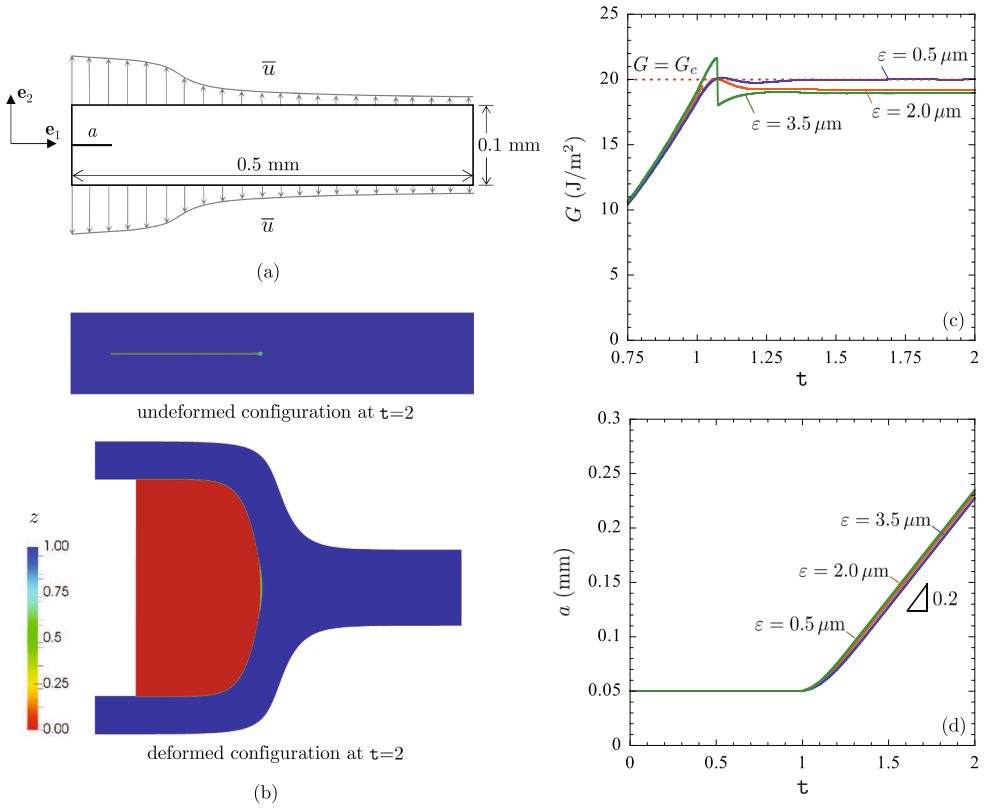

Fig. 5. Propagation of a crack along a straight path in a mode–I "surfing" boundary-value problem as predicted by the phase-field model (6) and (7) with external driving force (22) and coefficients (24). (a) Schematic of the "surfing" boundary-value problem (thickness 0.02 mm) for the boundary condition (32) and (33) with $V = 0.2$ mm, $t^* = 1.0$, $A = 0.15$ mm, and $d = 0.05$ mm. (b) Contour plots of the phase field z in the undeformed and deformed configurations at time t = 2 for the simulation with localization length $\varepsilon = 2.0$ μm. (c) The energy release rate G as a function of time t for three decreasing values of the localization length ε. (b) The corresponding crack length a as a function of time t. The results pertain to the same PDMS elastomer considered in Figs. 3 and 4.

completeness, Fig. 5(b) shows contour plots of the phase field z in the undeformed and deformed configurations at t = 2, when the crack has grown to a length of $a = 0.23$ mm, for the simulation with localization length $\varepsilon = 2.0$ μm.

The two main observations from Fig. 5(d) are that the pre-existing crack starts propagating at about t = t* = 1 and that by around t = 1.2 subsequent loading results in its "steady-state" propagation at the prescribed constant "velocity" $V = 0.2$ mm, irrespectively of the value of the localization length ε. The main observation from Fig. 5(c) is that the "steady-state" propagation of the crack for t > 1.2 is associated with a constant value of the energy release rate G that is roughly equal to the critical energy release rate G_c. More specifically, all three localization lengths ε deliver values of G that are within 5% of G_c to which they appear to converge as ε decreases, confirming that the phase-field model (6) and (7) with external driving force (22), coefficients (24), and a properly calibrated value of α^ε- predicts the same crack propagation as that dictated by the Griffith competition between bulk elastic energy and surface fracture energy, as desired.

5. 3D simulations of rubber bands under tension

In this last section, we showcase the capabilities of the proposed phase-field model (6) and (7), with external driving force (22) and coefficients (24), to describe the nucleation and propagation of fracture in rubber bands subject to tensile loading.

Specifically, as schematically depicted by Fig. 6, we consider rubber bands of circular cross- with initial diameter $d_0 = 2$ mm and three different initial lengths $l_0 = d_0/35 = 0.057$ mm, $l_0 = d_0/13.3 = 0.15$ mm, and $l_0 = 20 \times d_0 = 40$ mm. The bands are stretched by bonding their top and bottom boundaries to rigid plates which are pulled apart by a prescribed displacement u. The corresponding force required to do so is denoted by P. For consistency with the experimental literature, the results below are presented in terms of the "global" stretch λ and the "global" nominal stress s, which are defined in terms of u and P by the relations $\lambda = 1 + u/l_0$ and $s = 4P/(\pi d_0^2)$.

These particular types of geometries and boundary conditions are selected because they are representative of two famed experiments that are known to feature very different — and, for the cases of the very short and the short rubber bands, very complex — types of nucleation and propagation of fracture. Precisely, the very short ($l_0 = d_0/35$) and the short ($l_0 = d_0/13.3$) rubber bands are representative of thin and thick specimens used in the so-called poker-chip experiment; see, e.g., Busse [6], Gent and Lindley [15], and Lindsey [29]. On the other hand, the long ($l_0 = 20 \times d_0$) rubber band is representative of specimens used in measuring tensile strength [41], which in turn, are representative of the celebrated rubber bands invented by Stephen Perry in the 1840s.

We emphasize that in this first deployment of the model, our goal is not to confront its predictions directly with experimental data, but to illustrate that the very different ways in which rubber bands can break depending on their geometry are all well described by the model. Direct quantitative comparisons with experiments, including the classical poker-chip experiments of Gent and Lindley [15] as well as new experiments of our own, will be reported elsewhere.

All three rubber bands are taken to be made of the same PDMS 30:1 Sylgard 184 elastomer considered in Figs. 3 and 4. Accordingly, their elasticity is characterized by the stored-energy function (8) with material parameters $\mu_1 = 0.03192$ MPa, $b_1 = 1.39107$, $\mu_2 = 0.01857$ MPa, $b_2 = -1.02103$, and $\kappa = 10^3(\mu_1 + \mu_2) = 50.49$ MPa. Their strength is taken to be characterized by the surface (20) with parameters (21) for constant uniaxial tensile strength $s_{ts} = 0.41$ MPa and spatially random

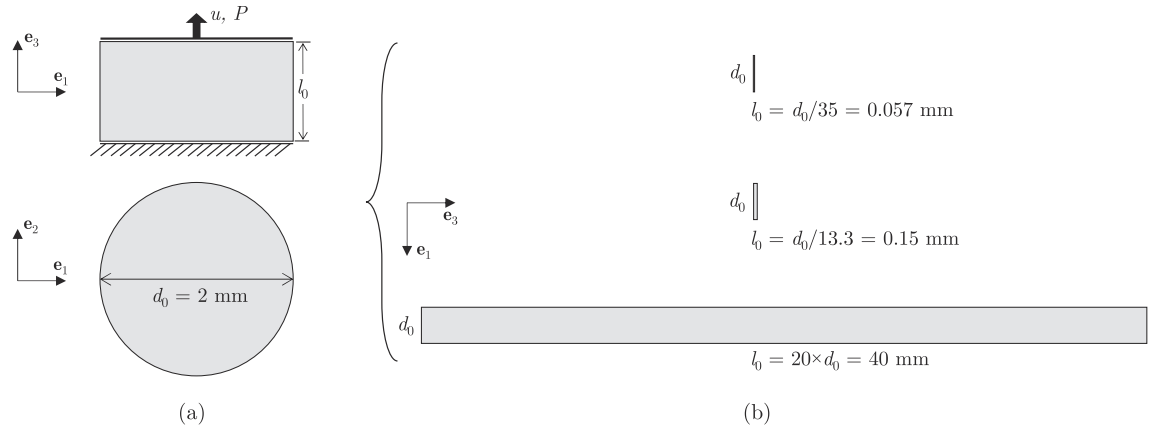

Fig. 6. (a) Schematic of the initial geometry of the rubber bands and applied boundary conditions. (b) Size comparison to scale of the very short ($l_0 = d_0/35 = 0.057$ mm), the short ($l_0 = d_0/13.3 = 0.15$ mm), and the long ($l_0 = 20 \times d_0 = 40$ mm) rubber bands.

heterogeneous hydrostatic tensile strength taking values in the set $s_{\text{hs}} = \{0.45, 0.50, 0.55\}$ MPa; as it will become apparent below, this mild stochasticity suffices to make contact with one of the key observations in thin poker-chip experiments. Finally, the critical energy release rates of all three rubber bands are taken to be given by $G_c = 20$ J/m^2 and $k_{\mathcal{H}} = 0$; see the Appendix.

The resulting governing Eqs. (6) and (7) for the above-outlined boundary-value problems are solved by means of the finite-element scheme introduced in Section 4 of Kumar et al. [23]. All simulations presented below are generated by making use of a uniform and unstructured Crouzeix–Raviart non-conforming finite-element discretization based on 4-node simplexes featuring an average diameter $h = \varepsilon/5$ and correspond to parameters $\eta_W = 10^{-3}$ and $\eta_\kappa = (\mu/\kappa)10^{-3} = 10^{-6}$. For relative computational frugality, exploiting the inherent symmetries, all simulations are also carried out over just one quarter of the rubber bands. Furthermore, the simulations for the very short and the short rubber bands correspond to a value of the localization length of $\varepsilon = 3.0$ μm, while the simulation for the long rubber band corresponds to $\varepsilon = 0.1$ mm; smaller values of ε were checked to produce essentially the same converged results. The associated values of the coefficient α^ε are taken to be constant (see Remark 15) and given by $\alpha^\varepsilon = 1.62$ for $\varepsilon = 3.0$ μm and $\alpha^\varepsilon = -8.1$ for $\varepsilon = 0.1$ mm.

5.1. The very short rubber band: $l_0 = d_0/35$

Fig. 7 presents results from the simulation for the very short rubber band. The line plot shows the stress s predicted by the phase-field model as a function of the applied stretch λ. On the other hand, the contour plots show the phase field predicted by the model at three increasing values of the applied stretch, $\lambda = 1.028$, 1.067, and 1.150. Precisely, for clearer visualization, three contour plots show the phase field $z(\mathbf{X}, t)$ across the midplane of the band, while the fourth one shows $z(\mathbf{X}, t)$ over an octant of the band at the indicated stretches λ. As implied by the spatial argument in the phase field $z(\mathbf{X}, t)$, all the contour plots are shown over the undeformed configuration of the band.

The key observation from the results presented in Fig. 7 is that fracture occurs exclusively around the midplane of the band, entirely within its bulk, in a cascading sequence of crack nucleation events that originates from the center and proceeds radially outward as the applied stretch λ increases. Precisely, two cracks are first nucleated around the center of the band at a stretch of about $\lambda = 1.028$. As λ increases, more cracks are sequentially nucleated radially away from the center at random locations. At the stretch of about $\lambda = 1.150$, cracks are already present throughout the entire midplane of the band, save for a boundary layer around its lateral traction-free boundary. In this process, it is of note that cracks are nucleated at random locations because of the assumed stochasticity of the hydrostatic tensile strength s_{hs}. Once a crack is nucleated, it exhibits limited subsequent stable propagation, instead the nucleation of more cracks is preferred as λ increases. It is also of note that the nucleation of cracks and their subsequent propagation result in a stress s that roughly remains plateaued at around $s = 0.3$ MPa as the stretch λ increases.

All the above-outlined theoretical predictions are consistent with the experimental observations reported in the literature for thin poker-chip experiments; cf. the results in Figs. 1 and 4 reported in [15] and Section 3.3 in [27].

5.2. The short rubber band: $l_0 = d_0/13.3$

Fig. 8 presents results for the short rubber band that are entirely analogous in format to those presented in Fig. 7 for the very short rubber band.

Similar to the first nucleation event in the very short rubber band, a single crack nucleates around the center of the short rubber band, albeit at the significantly larger stretch of about $\lambda = 1.083$. As the applied stretch λ increases, by contrast, no more cracks are nucleated, instead, the sole crack nucleated near the center of the band propagates first vertically in the direction of the applied load and then radially outward. The point at which the crack nucleates shows markedly as a drop in the stress-stretch response. The subsequent propagation of the crack does also provide for a sufficiently strong softening mechanism that keeps the stress s roughly plateaued with further applied stretch λ.

Much like those presented in Fig. 7, all the theoretical predictions presented in Fig. 8 are too consistent with the experimental observations reported in the literature for thick poker-chip experiments; cf. the results in Figs. 1 and 4 reported in [15] and Section 3.3 in [27].

5.3. The long rubber band: $l_0 = 20 \times d_0$

Finally, Fig. 9 reports results from the simulation for the long rubber band. The line plot shows the predicted stress s as a function of the applied stretch λ, while the contour plot shows the predicted phase field $z(\mathbf{X}, t)$ over the entire specimen at the applied stretch $\lambda = 4.01$. The latter includes an inset that zooms in the region of the band where a crack nucleates.

In stark contrast with the two preceding sets of results, as expected from the experience of playing with rubber bands and consistent with the experimental observations reported in the literature on the tensile strength of elastomers [41], the results in Fig. 9 show that the long rubber band stretches uniformly — save for, of course, the localized heterogeneous stretching taking place near its top and bottom boundaries because of the bonding to rigid plates — until an applied stretch of about $\lambda = 4.01$, at which point a crack nucleates abruptly across the band severing it in two pieces.

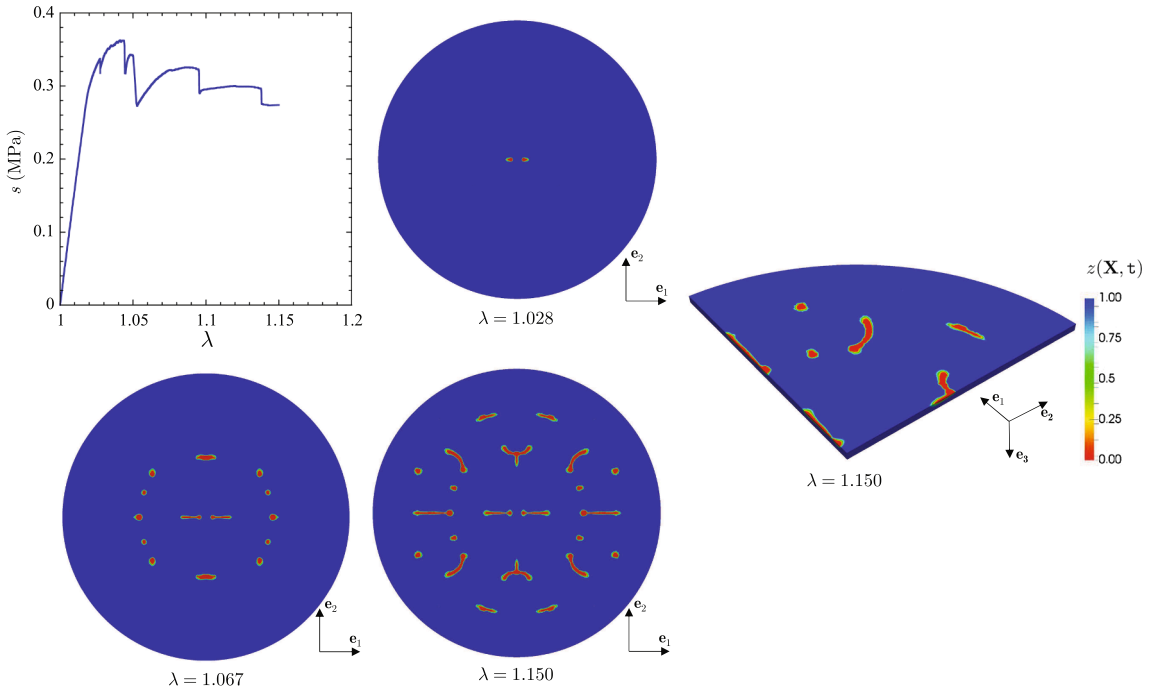

Fig. 7. 3D simulation of the very short ($l_0 = d_0/35 = 0.057$ mm) rubber band under tension. The line plot shows the predicted stress s as a function of the applied stretch λ. The contour plots show the predicted phase field $z(\mathbf{X}, t)$ across the midplane of the band at three different applied stretches, $\lambda = 1.028$, 1.067, 1.150, and over an octant of the band at $\lambda = 1.150$.

It is important to note here that the location where the crack nucleates in the simulations for the long rubber band is controlled by two factors, both physical: (*i*) the localized heterogeneity of the elastic fields near the top and bottom boundaries and (*ii*) the stochasticity of the strength of the rubber. Regardless of the strength stochasticity, because of the concentration of the stress fields near the top and bottom boundaries, the crack always nucleates either near the top or the bottom boundary. Whether it is the top or the bottom depends on the strength stochasticity; in the simulation presented in Fig. 9, the crack happens to nucleate near the bottom boundary.

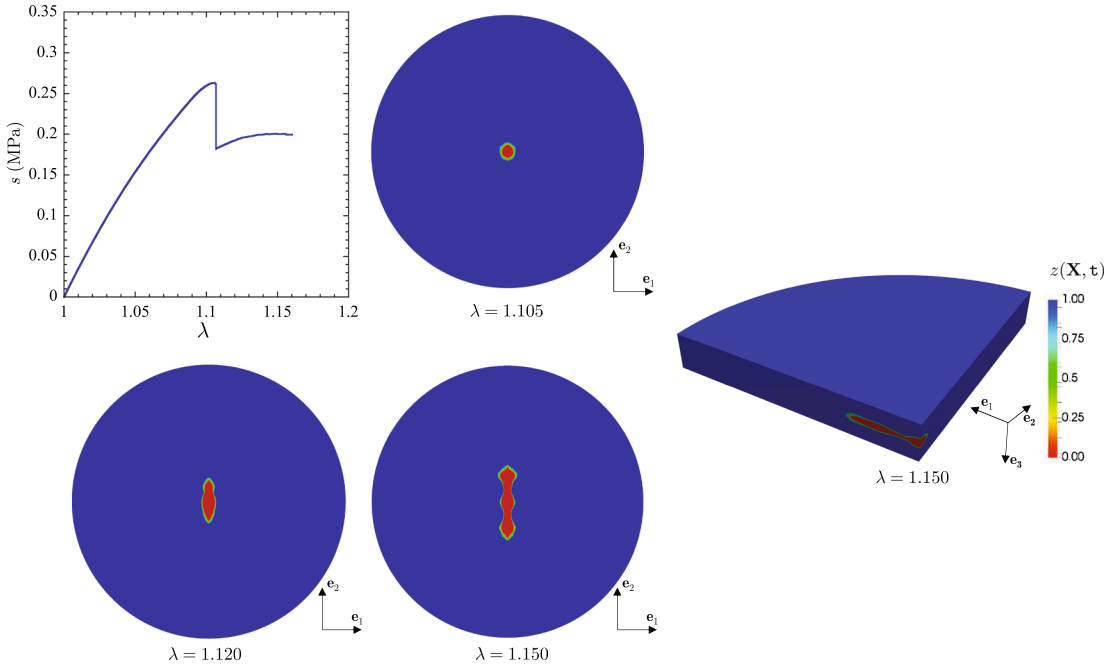

Fig. 8. 3D simulation of the short ($l_0 = d_0/13.3 = 0.15$ mm) rubber band under tension. The line plot shows the predicted stress s as a function of the applied stretch λ. The contour plots show the predicted phase field $z(\mathbf{X}, t)$ across the midplane of the band at three different applied stretches, $\lambda = 1 = 1.083$, 1.120, 1.150, and over a quarter of the band at $\lambda = 1.150$.

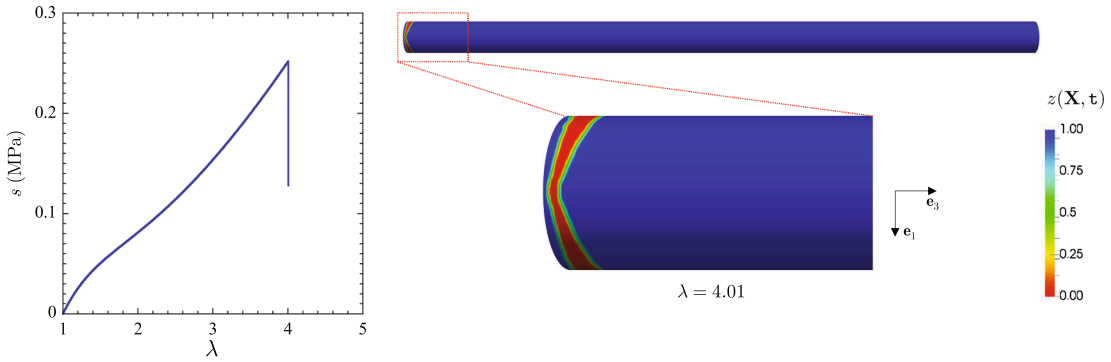

Fig. 9. 3D simulation of the long ($l_0 = 20 \times d_0 = 40$ mm) rubber band under tension. The line plot shows the predicted stress s as a function of the applied stretch λ. The contour plot shows the predicted phase field $z(\mathbf{X}, t)$ over the entire band at $\lambda = 4.01$.

Declaration of interests

The authors declare that they have no known competing financial interests or personal relationships that could have appeared to influence the work reported in this paper.

CRediT authorship contribution statement

Aditya Kumar: Conceptualization, Methodology, Software, Writing - original draft, Writing - review & editing. **Oscar Lopez-Pamies:** Conceptualization, Methodology, Supervision, Writing - original draft, Writing - review & editing, Funding acquisition.

Declaration of Competing Interest

The authors declare that they have no known competing financial interests or personal relationships that could have appeared to influence the work reported in this paper.

Acknowledgements

Support for this work by the National Science Foundation through the Grants DMS–1615661 and CMMI–1901583 are gratefully acknowledged.

Appendix A. The elasticity, strength, and critical energy release rate of PDMS 30:1

In this appendix, we outline the calibration process of the three material inputs — namely, $\mathcal{W}(\mathbf{F})$, $\mathcal{T}(\mathbf{S})$, and G_c — that go into the proposed model for a given elastomer of interest. We do so by way of an example and focus in particular on the PDMS Sylgard 184 elastomer with weight ratio 30:1 of base to curing agent for which the results in Figs. 2–5 and Figs. 7–9 pertain to. As mentioned in the main body of the text, such an elastomer is one of six different elastomers recently investigated by Poulain et al. [37,38].

We begin by calibrating the stored-energy function $\mathcal{W}(\mathbf{F})$ that describes the elasticity of the elastomer. To that end, we choose $\mathcal{W}(\mathbf{F})$ to be given by the Lopez-Pamies stored-energy function (8) and determine its five material parameters μ_1, b_1, μ_2, b_2, and κ by fitting the stress-stretch (S-λ) data reported by Poulain et al. [37] for the quasistatic uniaxial tension of a thin specimen with rectangular cross section. Such a fitting process renders the values indicated in the main body of the text, that is, $\mu_1 = 0.03192$ MPa, $b_1 = 1.39107$, $\mu_2 = 0.01857$ MPa, $b_2 = -1.02103$, $\kappa = 10^3(\mu_1 + \mu_2) = 50.49$ MPa. Fig. 10(a) compares the stress-stretch relation predicted by model directly with the experimental data. It is plain that the model is in good agreement with the experiment for the entire range of applied stretches up to the point at which the specimen breaks; more on this below. We also remark that the obtained fitted parameters render a stored-energy function (8) that is strictly

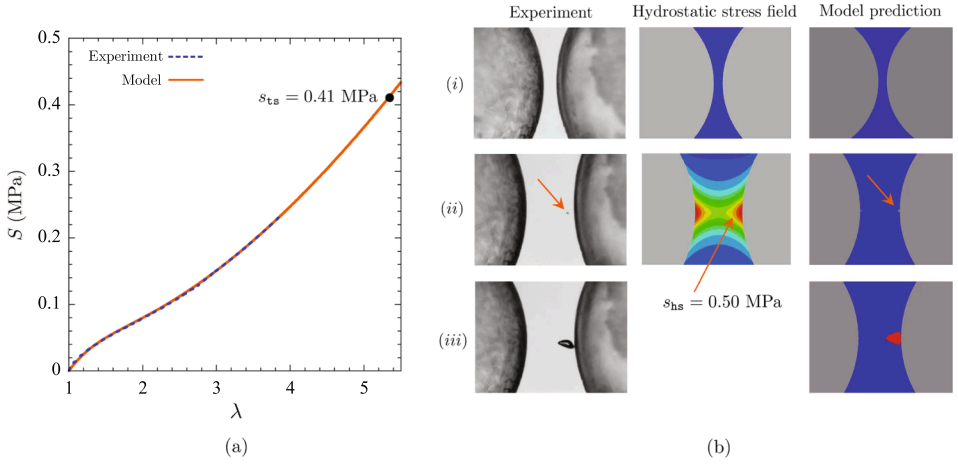

Fig. 10. Calibration of the elasticity and the strength of PDMS 30:1. (a) Stress-stretch response in quasistatic uniaxial tension of PDMS 30:1. The dashed line corresponds to an experiment of Poulain et al. [37], while the solid line corresponds to its fit with the Lopez-Pamies model (8). The specimen in the experiment broke near the grips at an applied stretch of about $\lambda = 3.9$ and corresponding stress of $S = 0.24$ MPa. The intrinsic tensile strength is estimated to be $s_{ts} = 0.41$ MPa. (b) Snapshots of a "two-particle" experiment of Poulain et al. [38] in which the nucleation of a crack in PDMS 30:1 occurs — by design — at a material point subject to almost purely hydrostatic tensile stress. A full-field elastic simulation up to the point of nucleation allows to extract from direct comparison with the experiment that the hydrostatic tensile strength of PDMS 30:1 is approximately given by $s_{hs} = 0.50$ MPa. For further direct comparison, the figure reproduces snapshots from Kumar et al. [24] of the simulation of the experiment as predicted by the model with external driving force (17).

polyconvex and hence strongly elliptic; see Section 3 in Lopez-Pamies [30].

We proceed by calibrating the function $\mathcal{F}(\mathbf{S})$ that describes the strength of the elastomer. To do so, we choose $\mathcal{F}(\mathbf{S})$ to be given by the Drucker-Prager function (20) and determine its two material parameters γ_1 and γ_2 in terms of the uniaxial tensile strength $s_{\rm ts}$ obtained from the uniaxial tension experiment of Poulain et al. [37] and of the hydrostatic tensile strength $s_{\rm hs}$ obtained from a "two-particle" experiment of Poulain et al. [38]; recall that in terms of $s_{\rm ts}$ and $s_{\rm hs}$, the material parameters γ_1 and γ_2 are given by relations (21).

Now, as shown by Fig. 10(a), the specimen in the uniaxial tension experiment of Poulain et al. [37] broke at an applied stretch of about $\lambda = 3.9$ and corresponding stress of $S = 0.24$ MPa. The latter value does *not* correspond to the actual tensile strength of PDMS 30:1, as the specimen broke outside the gauge section near the grips because of the concentration of stress there and the likely presence of geometric defects on its surface. Avoiding fracture taking place outside the gauge section, where the stress fields are *not* uniform, is a well-known challenge in the characterization of the tensile strength of elastomers since the pioneering work of Smith [41]; a possible solution may be the use of ring specimens with circular cross section. At any rate, the maximum value $S = 0.24$ MPa of the stress reached in the experiment serves to establish that $s_{\rm ts} > 0.24$ MPa for PDMS 30:1. In this work, for definiteness, we choose $s_{\rm ts} = 0.41$ MPa. As shown by Fig. 10(a), according to the model utilized to describe its elasticity, this value entails that PDMS 30:1 can be stretched up to $\lambda = 5.3$ in uniaxial tension, which is in the ballpark of standard elastomers [41].

Fig. 10(b) shows three snapshots of the "two-particle" experiment on PDMS 30:1 reported by Poulain et al. [38]; see Fig. 2 in that reference for an entire sequence of snapshots. It shows the region of the transparent PDMS 30:1 elastomer in between two firmly embedded glass particles: (*i*) in the undeformed configuration, (*ii*) at the point during the applied loading at which a crack first nucleates (indicated by an arrow), and (*iii*) right after the nucleation event, when the crack has propagated a few microns. By design, the stress fields in the elastomer near the glass particles are almost purely hydrostatic (in tension) prior to the nucleation of a crack. A full-field elastic simulation of the experiment — assuming that the PDMS 30:1 elastomer is characterized by the stored-energy function (8) calibrated above — confirms that is indeed the case and, more importantly, allows to deduce by direct comparison with the experiment that the hydrostatic tensile strength of PDMS 30:1 is given approximately by $s_{\rm hs} = 0.50$ MPa.

Finally, we turn to calibrating the critical energy release rate G_c of the elastomer. Poulain et al. [38] carried out a plurality of mechanical tests on PDMS 30:1 that established that this material does not exhibit any significant Mullins effect or viscous dissipation and hence that it can be considered as purely elastic for all practical purposes. However, they did not carry out tests to measure its toughness. From the classical work of Lake and Thomas [26], notwithstanding, one can estimate that the critical energy release rate of PDMS 30:1 is between 10 and 100 J/m^2. In this work, for definiteness, we choose $G_c = 20$ J/m^2.

Appendix B. Supplementary material

Supplementary data associated with this article can be found, in the online version, at https://doi.org/10.1016/j.tafmec.2020.102550.

References

[1] L. Ambrosio, V.M. Tortorelli, Approximation of functionals depending on jumps by elliptic functionals via Γ-convergence, Commun. Pure Appl. Math. 43 (1990) 999–1036.
[2] H. Amor, J.-J. Marigo, C. Maurini, Regularized formulation of the variational brittle fracture with unilateral contact: Numerical experiments, J. Mech. Phys. Solids 57 (2009) 1209–1229.
[3] E.M. Arruda, M.C. Boyce, A three-dimensional constitutive model for the large stretch behavior of rubber elastic materials, J. Mech. Phys. Solids 41 (1993) 389–412.
[4] B. Bourdin, G.A. Francfort, J.J. Marigo, Numerical experiments in revisited brittle fracture, J. Mech. Phys. Solids 48 (2000) 797–826.
[5] B. Bourdin, G.A. Francfort, J.J. Marigo, The variational approach to fracture, J. Elast. 91 (2008) 5–148.
[6] W.F. Busse, Physics of rubber as related to the automobile, J. Appl. Phys. 9 (1938) 438–451.
[7] A. Chambolle, S. Conti, G.A. Francfort, Approximation of a brittle fracture energy with a constraint of non-interpenetration, Arch. Rat. Mech. Anal. 228 (2018) 867–889.
[8] R.A. Dickie, T.L. Smith, Ultimate tensile properties of elastomers. VI. Strength and extensibility of a styrene–butadiene rubber vulcanizate in equal biaxial tension, J. Polym. Sci. A-2 Polym. Phys. 7 (1969) 687–707.
[9] D.C. Drucker, W. Prager, Soil mechanics and plastic analysis for limit design, Q. Appl. Math. 10 (1952) 157–165.
[10] C.W. Extrand, A.N. Gent, Strength under various modes of deformation, Int. J. Fracture Mech. 48 (1991) 281–297.
[11] G.A. Francfort, J.J. Marigo, Revisiting brittle fracture as an energy minimization problem, J. Mech. Phys. Solids 46 (1998) 1319–1342.
[12] G.A. Francfort, A. Giacomini, O. Lopez-Pamies, Fracture with healing: a first step towards a new view of cavitation, Anal. PDE 12 (2019) 417–447.
[13] A.N. Gent, Cavitation in rubber: a cautionary tale, Rubber Chemist. Technol. 63 (1990) 49–53.
[14] A.N. Gent, A new constitutive relation for rubber, Rubber Chem. Technol. 69 (1996) 59–61.
[15] A.N. Gent, P.B. Lindley, Internal rupture of bonded rubber cylinders in tension, Proc. R. Soc. A 249 (1959) 195–205.
[16] A.N. Gent, B. Park, Failure processes in elastomers at or near a rigid inclusion, J. Mater. Sci. 19 (1984) 1947–1956.
[17] A.N. Gent, W.V. Mars, Strength of elastomers, in: J.E. Mark, B. Erman, C.M. Roland (Eds.), The Science and Technology in Rubber, Elsevier, 2013.
[18] A.A. Griffith, The phenomena of rupture and flow in solids, Philos. Trans. R. Soc. Lond. A 221 (1921) 163–198.
[19] M.E. Gurtin, Generalized Ginzburg-Landau and Cahn-Hilliard equations based on a microforce balance, Physica D 92 (1996) 178–192.
[20] A. Hoger, D.E. Carlson, Determination of the stretch and rotation in the polar decomposition of the deformation gradient, Q. Appl. Math. 42 (1984) 113–117.
[21] M.Z. Hossain, C.-J. Hsueh, B. Bourdin, K. Bhattacharya, Effective toughness of heterogeneous media, J. Mech. Phys. Solids 71 (2014) 320–348.
[22] I.D. Johnston, D.K. McCluskey, C.K.L. Tan, M.C. Tracey, Mechanical characterization of bulk Sylgard 184 for microfluidics and microengineering, J. Micromech. Microeng. 24 (2014) 035017.
[23] A. Kumar, G.A. Francfort, O. Lopez-Pamies, Fracture and healing of elastomers: a phase-transition theory and numerical implementation, J. Mech. Phys. Solids 112 (2018) 523–551.
[24] A. Kumar, K. Ravi-Chandar, O. Lopez-Pamies, The configurational-forces view of fracture and healing in elastomers as a phase transition, Int. J. Fract. 213 (2018) 1–16.
[25] Kumar, A., Bourdin, B., Francfort, G.A., Lopez-Pamies, O., 2020. Revisiting nucleation in the phase-field approach to brittle fracture. In preparation.
[26] G.J. Lake, A.G. Thomas, The strength of highly elastic materials, Proc. Roy. Soc. A 300 (1967) 108–119.
[27] V. Lefèvre, K. Ravi-Chandar, O. Lopez-Pamies, Cavitation in rubber: an elastic instability or a fracture phenomenon? Int. J. Fract. 192 (2015) 1–23.
[28] M. Leonard, N. Wang, O. Lopez-Pamies, T. Nakamura, The nonlinear elastic response of filled elastomers: experiments vs. theory for the basic case of particulate fillers of micrometer size, J. Mech. Phys. Solids 135 (2020) 103781.
[29] G.H. Lindsey, Triaxial fracture studies, J. Appl. Phys. 38 (1967) 4843–4852.
[30] O. Lopez-Pamies, A new I_1-based model for rubber elastic materials, C.R. Mec. 338 (2010) 3–11.
[31] E. Lorentz, A nonlocal damage model for plain concrete consistent with cohesive fracture, Int. J. Fract. 207 (2017) 123–159.
[32] C. Miehe, F. Welschinger, M. Hofacker, Thermodynamically consistent phase-field models of fracture: variational principles and multi-field FE implementations, Int. J. Numer. Meth. Eng. 83 (2010) 1273–1311.
[33] M.P. Milner, L. Jin, S.B. Hutchens, Creasing in evaporation-driven cavity collapse, Soft Matter 13 (2017) 6894–6904.
[34] S. Narayan, L. Anand, A gradient-damage theory for fracture of quasi-brittle materials, J. Mech. Phys. Solids 129 (2019) 119–146.
[35] Q.S. Nguyen, S. Andrieux, The non-local generalized standard approach: a consistent gradient theory, C.R. Mec. 333 (2005) 139–145.

[36] K. Pham, H. Amor, J.J. Marigo, C. Maurini, Gradient damage models and their use to approximate brittle fracture, Int. J. Damage Mech. 20 (2011) 618–652.
[37] X. Poulain, V. Lefèvre, O. Lopez-Pamies, K. Ravi-Chandar, Damage in elastomers: nucleation and growth of cavities, micro-cracks, and macro-cracks, Int. J. Fract. 205 (2017) 1–21.
[38] X. Poulain, O. Lopez-Pamies, K. Ravi-Chandar, Damage in elastomers: healing of internally nucleated cavities and micro-cracks, Soft Matter 14 (2018) 4633–4640.
[39] R.S. Rivlin, A.G. Thomas, Rupture of rubber. Part I. Characteristic energy for tearing, J. Polym. Sci. 10 (1953) 291–318.
[40] P. Sicsic, J.J. Marigo, From gradient damage laws to Griffith's theory of crack propagation, J. Elast. 113 (2013) 55–74.
[41] T.L. Smith, Ultimate tensile properties of elastomers. II. Comparison of failure envelopes for unfilled vulcanizates, J. Appl. Phys. 35 (1964) 27–36.
[42] T.L. Smith, J.A. Rinde, Ultimate tensile properties of elastomers. V. Rupture in constrained biaxial tensions, J. Polym. Sci. A-2 Polym. Phys. 7 (1969) 675–685.
[43] D.J. Steigmann, Invariants of the stretch tensors and their application to finite elasticity theory, Math. Mech. Solids 7 (2002) 393–404.
[44] E. Tanné, T. Li, B. Bourdin, J.J. Marigo, C. Maurini, Crack nucleation in variational phase-field models of brittle fracture, J. Mech. Phys. Solids 110 (2018) 80–99.
[45] L.R.G. Treloar, The elasticity of a network of long-chain molecules — II, Trans. Faraday Soc. 39 (1943) 241–246.